Magnetic Resonance Electric Impedance Tomography for Anisotropic Conductivity Distribution

Rho Malik Loving
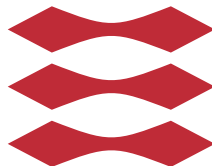
Summary (English)

The goal of the thesis is to investigate the problem of having an anisotropic conductivity distribution when working with impedance image reconstruction for Magnetic Resonance Electrical Impedance Tomography(MREIT).

The underlying physics of MREIT is introduced with the aim to show how an actual MREIT experiment would occur. Two models describing the forward problem of having known conductivity distribution and attaining the resultant z-component of the induced magnetic field are investigated. A simplified geometry for the conducting media is assumed to ease computational efforts and complexity of the reconstruction. The conducting media is assumed to have known sub-domains with different conductivity. A L-BFGS-B optimization algorithm is applied to solve the resultant non-linear constrained optimization problem of recovering the conductivity distribution.

Several aspects are investigated, including accuracy, sensitivity on initial guess, sensitivity on contrast between conductivities of the sub-domains and gain from adding more data. It is shown that using a general optimization scheme for finding anisotropic conductivity distributions when applying MREIT is a viable method where, when the choice of initial guess is good, the estimated parameters only suffer from a few % relative error. There is shown to be a threshold of needing at least three pairs of electrodes for viable estimation. It is shown that the geometry of the interior sub-domains influence the estimated parameters. Furthermore, it is shown that high contrast between conductivities of interior sub-domains produce a small bias in the estimated parameters.

Summary (Danish)

Målet for denne afhandling er at undersøge problemet ved at have en anisotropisk ledningsevnefordeling når der arbejdes med impedans billed rekunstruktion for Magnetisk Ressonans Elektrisk Impedans Tomografi(MREIT).

Den underliggende fysik, der beskriver MREIT bliver introduceret med det mål at vise, hvorledes et ægte MREIT experiment ville fungere. To modeller, der beskriver fremad problemet ved at have en kendt ledningsevnefordeling og opnå den resulterende z-komponent af det inducerede magnetfelt, bliver undersøgt. En simplifiseret geometri for det ledende medie bliver antaget for at lette beregninger og kompleksitet af rekonstruktionen. Der bliver antaget, at det ledende medie har kendte under-inddelinger med forskellige ledningsevner. En L-BFGS-B optimeringsalgoritme bliver anvendt til at løse det resulterende ikke-lineære begrænsede optimeringsproblem i at genskabe ledningsevnefordelingen.

Flere aspekter bliver undersøgt inkluderende akkurathed, sensitivitet på startgæt, sensitivitet på kontrast mellem ledningsevner i under-inddelingerne samt udbytte af at tilføje mere data. Det bliver vist, at det at bruge et generelt optimeringsskema til at finde anisotropiske ledningsevnefordelinger, når der anvendes MREIT er en brugbar metode, som når valget af startgæt er godt, så lider de estimerede parametre kun af få % relativ fejl. Der bliver vist at være en grænse ved at skulle bruge mindst tre elektrodepar for brugbar estimering. Der bliver vist at geometrien af de indre under-domæner har inflydelse på de estimerede parametre. Derudover bliver det vist, at en høj kontrast mellem ledningsevner i de indre under-domæner medfører et lille bias i de estimerede parametre.

Preface

This thesis was prepared at the department Compute at the Technical University of Denmark in fulfilment of the requirements for acquiring an M.Sc. in Mathematical Modelling.

The thesis deals with the subject of Magnetic Resonance Electrical Impedance Tomography(MREIT) and the pipeline that exists from experiment to image reconstruction.

The thesis consists of an introductory chapter which deals with the physics of the subject. Next follows a chapter on the forward problem of MREIT with focus on mathematical rigour. Then a chapter concerning the inverse problem of MREIT and finally a chapter containing experimental results.

Lyngby, 31-October-2013

Rho Malik Loving

Acknowledgements

Contents

Introduction

Magnetic Resonance Electrical Impedance Tomography(MREIT) is a conductivity image reconstruction modality which has been researched widely in the last decade. The method is a subcategory of the larger research area called coupled physics in which two connected physical modalities are used, one to excite the sought physiological quantity and one to measure the given excitement. MREIT was developed because the standard conductivity imaging modality of EIT has poor spatial resolution and is thus not applicable for steady state imaging which is required for diagnostics. However, EIT still shows great potential for time varying imaging like that of monitoring patients. In the case of MREIT, a MRI machine is used to measure the induced magnetic field originating from applying a current field through electrodes fastened on the exterior boundary. It has been shown in [WS11] that existence and uniqueness is guaranteed for 2D reconstruction of an isotropic conductivity distribution when only measuring the z-component of the induced magnetic field. In this case, stable algorithms, like the harmonic B_z-algorithm, has been utilized to reconstruct conductivity images[WS08]. The foremost front in MREIT in-vivo image reconstruction is that of the CoReHA 2.0 package [JL12]. The CoReHA 2.0 package aims to find a scaled isotropic conductivity distribution.

It is of great interest in medical imaging to be able to find the interior conductivity distribution of any part of the human body. Conductivity of tissue can help distinguish between healthy and unhealthy tissue. Besides, knowledge of the conductivity distribution in the brain would greatly improve any electro-shock

treatments that are being applied to counter neurological diseases.

In this thesis the modelling of an anisotropic conductivity distribution is attempted. This is done because some tissue types like bone, white-matter and muscle fibres show highly anisotropic conductivities. To do this, two forward models handling anisotropic conductivity for finding the potential distribution given some electrode configuration is presented and compared. From here on, the magnetic field induced by the current distribution is calculated for a simplified symmetric geometry which has some applicability to real experiments. It is assumed in this thesis that the boundaries of different tissue types inside the imaging object is known a priori from a regular MR image and based on that an optimization scheme is employed in the end to find the anisotropic conductivity distribution. Several different experiments highlighting strengths and weaknesses of the procedure is conducted and results are presented and discussed.

Maxwell's equations and Impedance Imaging

As the thesis concerns the topic of Magnetic Resonance Electrical Impedance Tomography, it is an obvious starting point, theoretically to introduce Maxwell's equations, the governing equations of electromagnetism. For time varying systems, they are as follows [YFF11]:

$$\nabla \times \mathbf{E} = -\frac{\partial \mathbf{B}}{\partial t}, \tag{2.1}$$

$$\nabla \cdot \mathbf{D} = \rho, \tag{2.2}$$

$$\nabla \times \mathbf{H} = \mathbf{J} + \frac{\partial \mathbf{D}}{\partial t}, \tag{2.3}$$

$$\nabla \cdot \mathbf{B} = 0. \tag{2.4}$$

Here all bold capital letters refer to vector fields and specifically, $\mathbf{E}$ is the electric field, $\mathbf{B}$ the magnetic flux density, $\mathbf{H}$ is the strength of the magnetic field, $\mathbf{D}$ is the displacement field and $\mathbf{J}$ is the current density field. The vector fields, $\mathbf{H}$, $\mathbf{B}$, $\mathbf{J}$, $\mathbf{E}$ and $\mathbf{D}$ are connected in linear[1] conducting media such as biological tissue, through three constitutive equations given as follows [YFF11]:

---

[1] Linear is understood in the usual manner of linear addition, multiplication etc.

$$\mathbf{J} = \sigma\mathbf{E}, \qquad (2.5)$$

$$\mathbf{B} = \mu\mathbf{H}, \qquad (2.6)$$

$$\mathbf{D} = \epsilon\mathbf{E}. \qquad (2.7)$$

Here, $\sigma = \sigma(x,t)$ is the conductivity, $\epsilon = \epsilon(x,t)$ is the permittivity and $\mu = \mu(x,t)$ is the permeability. These three parameters are all material dependent and in this formulation, the media is linear which means that the parameters do not depend on the vector fields. Usually, the parameters are considered as scalar, however, there are certain forms of tissue, for instance muscle, which show anisotropic behaviour. The three parameters are generally dependent on the frequency of the electrical field, however, since the frequency can be chosen to not be time dependent, this frequency dependency can be omitted from the arguments. It is, however, important to have in mind that the frequency of the electric field has an influence on the parameters, as the goal of this thesis is conductivity image reconstruction and thus, the resulting reconstructed picture will be dependent on the frequency of the applied electrical field. Figure 2.1 depicts the conductivity for several different tissue types dependent on the frequency of the applied electric field.
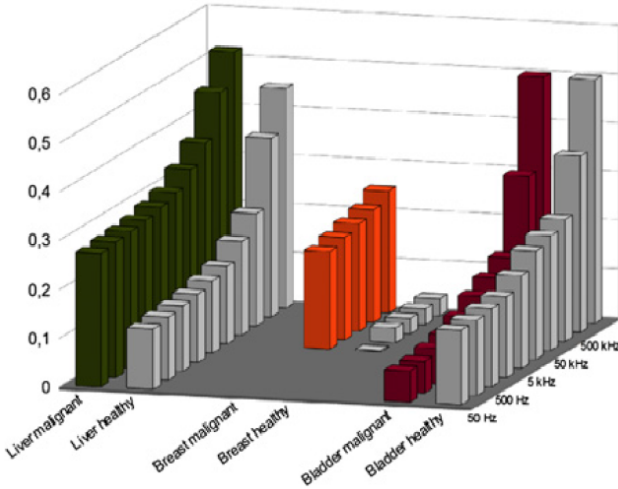

Figure 2.1: Isotropic conductivity given the frequency of the applied electric field for several tissue types.The figure is originally from [WS12]

Besides the fact that different tissue types exhibit different conductivities, figure 2.1 shows that malignant, in this case cancerous cells originating from these dif-

ferent tissue types, also show a distinct difference in conductivity compared to the non-malignant tissue surrounding the cancerous cells. Besides, it can be seen that the difference between malignant and non-malignant tissue, conductivity-wise, depends on the frequency of the electric field and that the difference is not necessarily linear. This can best be seen from the far most right comparison between malignant- and non-malignant bladder tissue, where the difference becomes smaller the higher the frequency of the applied electric field.

2.1 Impedance Imaging

The above section revealed that different materials exhibit different conductivity distributions. Thus, it is possible to identify types of material by knowledge of their conductivity. This has lead to a large field of research in the area of impedance imaging in which it is sought to find the interior conductivity distribution from measurements. Perhaps the most famous of these research areas is Electrical Impedance Tomography(EIT) in which boundary current/voltage measurements are used to construct the interior conductivity distribution. However, the inverse problem that arises from this model set up is extremely ill-posed and results exhibit poor spatial contrast in time independent imaging. However, since knowing the conductivity distribution appears to be a lucrative information, the search for a robust conductivity imaging modality is continually being worked on and the area of coupled physics, in which MREIT is a sub-area, shows a great potential for attaining such a robust conductivity imaging modality.

2.2 Governing Equation

This section will show the derivation of the governing partial differential equation for modelling Maxwell's equations. There exists two ways of expressing the governing equation. One, which will be derived below, assumes that the fields are time independent and the other assumes that the fields are time harmonic. The resulting governing equation from the time harmonic fields will be introduced and shortly explained in the subsequent section.

2.2.1 Time Independent Equations

Assuming that the fields $\mathbf{B}$ and $\mathbf{D}$ are time independent, it is possible to set the time derivatives associated with equations (2.1) and (2.3) to zero, yielding the

system of equations below.

$$\nabla \times \mathbf{E} = 0, \tag{2.8}$$
$$\nabla \cdot \mathbf{D} = \rho, \tag{2.9}$$
$$\nabla \times \mathbf{H} = \mathbf{J}, \tag{2.10}$$
$$\nabla \cdot \mathbf{B} = 0. \tag{2.11}$$

From (2.8) we can see that the electric field, $\mathbf{E}$, is rotation free and thus, we can conclude from the identity $\nabla \times \nabla \mathbf{f} = 0$ for $\mathbf{f} \in \mathrm{C}^2$ that there exists an electric potential, u, such that[KH98]

$$\mathbf{E} = -\nabla u. \tag{2.12}$$

Inserting (2.5) and (2.12) into (2.10) and taking the divergence, then yields

$$-\nabla \cdot (\sigma \nabla u) = 0, \tag{2.13}$$

which is a partial differential equation which for associated boundary conditions on $\partial \Omega$ can be solved to find the potential, $u(\mathbf{x})$ in some domain $\Omega \in \mathbb{R}^N$.

2.2.2   Time harmonic equations

The above derivation can be done in another way (see Appendix D for specifics) yielding a somewhat different result. Instead of looking for time independent solutions to Maxwell's equations, we can look for time harmonic solutions. This results in the governing equation

$$-\nabla \cdot (\kappa \nabla u) = 0.$$

Here, $\kappa = \sigma + i\epsilon$ is the "complex conductivity". Thus, we can provide a governing PDE which results in a time harmonic solution. These are true even for dispersive media, i.e. media for which properties such as conductivity is frequency dependent. Whereas the former derivation holds only for non-dispersive media. In the setting of MREIT, high frequency currents are rarely applied which

means that the complex part of the complex conductivity is usually negligible. However, there are ongoing plans on exploring MREIT at the Larmor frequency which cannot be considered as low frequency currents. However, in this thesis only low frequency currents are applied which means that the complex part of the conductivity is ignored.

2.2.3 Divergence Form

In the following chapter, two models for finding the electric potential are investigated. One which the original paper had adapted to complex conductivity, but isotropic and one which uses non-complex but anisotropic conductivity. For the remainder of this thesis, $\sigma(\mathbf{x})$ is assumed to be anisotropic unless otherwise stated. More detail on this will follow in chapter 3.
The equation (2.13), can be seen to be composed of a second order partial differential operator acting on the unknown distribution,$u(\mathbf{x})$ resulting in a PDE in divergence form. Generally speaking, PDEs in divergence form are given in the form

$$Lu = -\sum_{i,j=1}^{n} \left(a^{ij}(\mathbf{x})u_{x_i}\right)_{x_j} + \sum_{i=1}^{n} b^i(\mathbf{x})u_{x_i} + c(\mathbf{x})u. \qquad (2.14)$$

In this case, however, both b and c are zero for all i, j. In the general setting, the b-term is associated with transport in the media and the c-term models any sources or sinks in the system. In chapter 3 existence and uniqueness will be proven for the two governing PDEs with associated boundary conditions. If a PDE can be presented in divergence form, then the natural way of proving existence and uniqueness is through the use of Lax-Milgram's lemma which can be found in A.1. The next few sections will cover the fundamental theory of the imaging modality, MRI, and will culminate in the combined theory of MRI and EIT in MREIT. First, Magnetic Resonance Imaging is introduced.

2.3 MRI

This section follows closely the theory presented in [WS12]. Magnetic Resonance Imaging(MRI), is a widely used medical imaging modality which offers very good image resolution of soft tissue, like muscle, brain matter, blood etc. MRI uses the application of sequences of externally applied magnetic fields to

magnetize the protons(H^+) in the tissue. This is why, soft tissue, i.e. tissue containing relatively much water, yields the best results when applying MRI as a medical imaging modality.

MRI visualizes the magnetization of nuclei, $\mathbf{M}(\mathbf{x}, t)$ when exposed to an externally induced sequence of magnetic fields, $\mathbf{B}(\mathbf{x}, t)$. The two quantities are related through the simplified Bloch equation,

$$\frac{\partial \mathbf{M}(\mathbf{x}, t)}{\partial t} = \gamma \mathbf{M}(x, t) \times \mathbf{B}(\mathbf{x}, t). \tag{2.15}$$

Here, γ is the gyromagnetic ratio and for a proton(Hydrogen) is given by $4.6 \times 10^7 T^{-1} s^{-1}$ or $26.75 \times 10^7 \frac{\text{rad}}{\text{Ts}}$, T being Tesla, s seconds. When applying a stationary magnetic field $B(x) = (0, 0, B(\mathbf{x}))$, in the z-direction and having initial magnetization, $M_0 = \mathbf{M}(\mathbf{x}, 0) = (M_0^x, M_0^y, M_0^z)^T$, one can obtain an analytic solution to the simplified Bloch equation (2.15) given by[WS12]

$$\mathbf{M}(\mathbf{x}, t) = \begin{pmatrix} M_0^x \cos(-\gamma B(\mathbf{x})t) + M_0^y \sin(-\gamma B(\mathbf{x})t) \\ M_0^x \sin(-\gamma B(\mathbf{x})t) + M_0^y \cos(-\gamma B(\mathbf{x})t) \\ M_0^z \end{pmatrix}. \tag{2.16}$$

From this identity, the rotation of the magnetization around the z-axis can be seen. Thus, applying a stationary magnetic field does not result in a stationary magnetization. Furthermore, the frequency defined through

$$\omega(x) = -\gamma \mathbf{B}(x), \tag{2.17}$$

is the so-called Larmor-frequency which has a crucial role in MR imaging. Now, a note on the choice of model for the relation between the magnetization and the magnetic field is needed. As mentioned, the "simplified" Bloch equation (2.15) is applied. This is adequate because we restrict our interest in the precissional motion of $\mathbf{M}$, i.e. we are interested in the motion of $\mathbf{M}$ with regards to material specific relaxation parameters.

Now, by introducing the static magnetic field, $\mathbf{B}_0 = (0, 0, B_0)$ we get the associated Larmor frequency, $\omega_0 = -\gamma B_0$. This, for Hydrogen and a magnetic field with the strength $|B_0| = 1.5T$ means that the Larmor frequency becomes $\omega_0 = 63.9MHz$. Now, by introducing a gradient field, given by

$$\mathbf{B}^G(\mathbf{x}) = (0, 0, \mathbf{G} \cdot \mathbf{x}), \tag{2.18}$$

and applying it together with the static magnetic field $\mathbf{B}_0$, the Larmor frequency becomes $\omega(\mathbf{x}) = \omega_0 - \gamma \mathbf{G} \cdot \mathbf{x}$. Now, let $\mathbf{B}(\mathbf{x})$ be a static magnetic field and $\mathbf{M}(\mathbf{x})$ be the resulting magnetization given by (2.15). Then the MRI signal is collected through voltage measurements in a detector coil, which satisfies [WS12]

$$V(t) \propto \int \mathbf{M}(\mathbf{x}) \cdot \mathbf{B}^{rec}(\mathbf{x}) d^3\mathbf{x}, \qquad (2.19)$$

where $\mathbf{B}^{rec}(\mathbf{x})$ is the Biot-Savart[2] magnetic field corresponding to a unit current in the coil. Assuming that $\mathbf{B}^{rec}(\mathbf{x}) = (r\cos(\theta_B), r\sin(\theta_B), 0)$ is a radio-frequency field[3] and inserting into (2.19) yields

$$V(t) \propto \int \mathbf{M}(\mathbf{x}) \cdot (r\cos(\theta_B), r\sin(\theta_B), 0) d^3\mathbf{x} \qquad (2.20)$$

$$= \int \begin{pmatrix} M_0^x \cos(\omega(\mathbf{x})t) - M_0^y \sin(\omega(\mathbf{x})t) \\ M_0^x \sin(\omega(\mathbf{x})t) + M_0^y \cos(\omega(\mathbf{x})t) \\ M_0^z \end{pmatrix} \cdot \begin{pmatrix} r\cos(\theta_B) \\ r\sin(\theta_B) \\ 0 \end{pmatrix} d^3\mathbf{x} \qquad (2.21)$$

$$= \int M_0^x r\cos(\omega(\mathbf{x})t)\cos(\theta_B) - M_0^y r\sin(\omega(\mathbf{x})t)\cos(\theta_B) + \qquad (2.22)$$

$$M_0^x r\sin(\omega(\mathbf{x})t)\sin(\theta_B) + M_0^y r\cos(\omega(\mathbf{x})t)\sin(\theta_B) d^3\mathbf{x}. \qquad (2.23)$$

Now, by applying the trigonometric identities given by

$$\cos(a - b) = \cos(a)\cos(b) + \sin(a)\sin(b) \quad \text{and} \qquad (2.24)$$

$$\sin(a + b) = \sin(a)\cos(b) + \cos(a)\sin(b), \qquad (2.25)$$

into (2.23), we get to the solution for the voltage measurements, up to some given constant

$$V(t) = K \int M_0 \sin(\omega(\mathbf{x})t + \theta_B - \phi_0) d^3\mathbf{x}. \qquad (2.26)$$

Here, we have used that the polar representation of the transverse magnetization can be represented in the complex plane as $M_0 e^{i\phi_0} = M_0^x + i M_0^y$ and K is a

---

[2]Biot-Savart's law can be seen in (3.66)

[3]Radio frequency fields arise from alternating currents in the radio-frequency spectra through a conductor and are able to pass through free space

fixed complex proportionality factor. Now, by multiplying with the reference fields, $\cos(\omega_0 t)$ and $\sin(\omega_0 t)$ and filtering, the MRI-signal is obtained and given by

$$S(t) = \int_{\mathbb{R}^3} M_0(\mathbf{x}) e^{i\phi_0(\mathbf{x})} e^{i\omega(\mathbf{x})t} d^3\mathbf{x}. \qquad (2.27)$$

As can be seen by the above relation, it is only necessary to have an expression for the signal through the quantity of M_0, and not $M(t)$. This is because the signal is only measured while a static magnetic field is applied. This is also the case when we move on to MREIT in a few sections. Now, as can be seen from (2.27), the MRI-signal depends both on $\omega(\mathbf{x})$ and on $\mathbf{M}$. Thus, when conducting MRI, both of these are varied to obtain the data. The actual obtaining of this MRI signal is done by sampling the Fourier domain, i.e. k-space. The following small section goes through the mathematics of an MRI sequence generation and how this MRI-signal is obtained.

2.3.1 MRI sequence design

For a general MRI pulse sequence, a superposition of magnetic fields are applied. This superposition is given by

$$\mathbf{B}(\mathbf{x}, t) = \mathbf{B}_0(\mathbf{x}) + \mathbf{B}_1(\mathbf{x}, t) + \mathbf{B}^G(\mathbf{x}, t), \qquad (2.28)$$

where $\mathbf{B}_0(\mathbf{x})$ is the static magnetic field applied in the previous section and $\mathbf{B}^G(\mathbf{x}, t)$ is a gradient field from the previous section. Furthermore, $\mathbf{B}_1(\mathbf{x}, t)$ is a radio-frequency field given by $\mathbf{B}_1(\mathbf{x}, t) = (B_1 \cos(\omega_1 t), B_1 \sin(\omega_1 t), 0)$. The MRI sequence then goes as following. $\mathbf{B}_0(\mathbf{x})$ is applied throughout the experiment and then at some time, t_0, $\mathbf{B}_1(\mathbf{x}, t)$ is applied to create a non-zero initial magnetization, M_0. Thus, at every spatial point, $\mathbf{x}$, where the resonance condition $\omega_1 = \omega(\mathbf{x})$ holds, the magnetization vector is flipped away 90 degrees from the z-axis. The analogy of an ultimately stable(i.e. it will not tip) spinning top which is poked from the side illustrates well what happens at this stage. This event creates a non-zero transverse magnetization, $M_0 e^{i\phi_0}$. Now, at the same time a gradient field, $\mathbf{B}^{G_z} = (0, 0, G_z)$ is applied, which restricts the resonance condition to a small slice around $z = z_0$ and thus, M_0 is only different from zero in this small region - Remembering that MRI images are based on slices through the z-axis, this is a necessary procedure. Next, $\mathbf{B}^{G_y}(\mathbf{x}, t)$ with

$\mathbf{G}_y = (0, G_y, 0)$ is applied for a certain time t'. This changes the Larmor frequency to $\omega(\mathbf{x}) = \omega_0 + G_y y$. When the time, t' has passed, the phase of the transverse magnetization has changed to $\phi_0 + t'G_y y$. These are the preparations done before the actual measurement takes place. Finally the gradient field, $\mathbf{B}^{G_x}(\mathbf{x}, t)$ is applied, with $\mathbf{G}_x = (G_x, 0, 0)$. This again changes the Larmor frequency to $\omega(\mathbf{x}) = \omega_0 + G_x x$. Meanwhile the MRI-signal is sampled. Figure 2.2 shows the above described MR sequence.
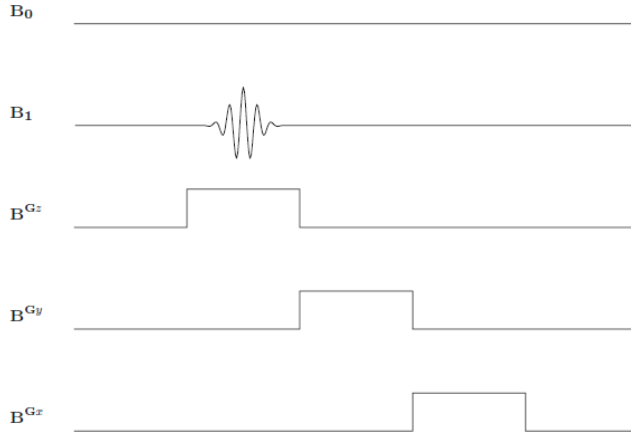
Figure 2.2: Standard MRI sequence, originally from [WS12]

Applying these three gradient fields allows the data sampling to only take place in a specific slice for which an image is supposed to be reconstructed and it allows the possibility to change the phase, ϕ_0 and the frequency, $\omega(\mathbf{x})$ of the transverse magnetization in 2D k-space, yielding the data

$$D(tG_x, t'G_y) = \int_{\mathbb{R}^2} M_0 e^{i\phi_0} e^{i\gamma(tG_x x + t'G_y y)} d(x, y). \qquad (2.29)$$

By introducing the 2D vector $\mathbf{k} = (tG_x, t'G_y)$, (2.29) is simply the 2D Fourier transform with respect to $\mathbf{k}$ of the transverse magnetization, $M_0(x, y, z_0)e^{i\phi_0}$. By repeating the sequence and varying the fields, G_x and G_y, one samples the Fourier transform,

$$\tilde{M} = \int_{\mathbb{R}^2} M_0 e^{i\phi_0} e^{i\gamma \mathbf{k} \cdot \mathbf{x}} d(x, y). \qquad (2.30)$$

Lastly, the inverse 2D Fourier transform allows the recovery of the MR image,

$M_0 e^{i\phi_0}$. It should be noted that the field $\mathbf{B}_1(\mathbf{x}, t)$ is directly affected by the electric properties of the human tissue which depends on $\sigma(\mathbf{x}, \omega_0)$. This can be utilized to recover the conductivity.

2.4   MREIT

Magnetic Resonance Electric Impedance Tomography (MREIT) is a relatively new imaging modality originating from the early 1990s. The frame work of MREIT is not very different from that of MRI, except MRI aims at constructing the Magnetization, $\mathbf{M}(\mathbf{x})$, whereas MREIT aims to reconstruct the conductivity distribution $\sigma(\mathbf{x})$. Early versions of MREIT needed all three components of the induced magnetic density field, $\mathbf{B}(\mathbf{x})$. However, given that this requires the imaging object to be rotated within the MR machine, it is highly inconvenient when the imaging object becomes large which is for instance the case of a human body. Furthermore, rotating the body introduces problems regarding errors in the positioning of electrodes, boundaries and, perhaps most importantly, the location of internal organs. If this rotation had been easy, it is possible to apply Ampere's law given by

$$\mathbf{J}(\mathbf{x}) = \frac{1}{\mu_0} \nabla \times \mathbf{B}(\mathbf{x}), \qquad (2.31)$$

to reconstruct the current distribution, $\mathbf{J}(\mathbf{x})$, inside the imaging object in all three components from which an algorithm called the $\mathbf{J}$-substitution method can be applied to find the conductivity distribution. However, it has been shown that even with phantom imaging objects, rotation within the MR machine resulted in significant errors and thus, bad reconstructions of conductivity distributions [WS11]. Hence, this practical problem was turned into a mathematical problem where only data from the B_z component must be utilized to reconstruct the conductivity distribution. The setup is very similar to that of MRI. Additionally to the MR machine, pairs of electrodes are placed on the surface of the imaging object through which currents are sequentially passed through. This probes a current density field inside the imaging object which is dependent on the conductivity distribution, $\sigma(\mathbf{x})$. From (2.31) we see that a current density field imposes the existence of a magnetic density field which will be called $\mathbf{B_J}(\mathbf{x})$ This field then acts as an extra gradient field in the superposition given in (2.28) and extends this to be

$$\mathbf{B}(\mathbf{x}, t) = \mathbf{B}_0(\mathbf{x}) + \mathbf{B}_1(\mathbf{x}, t) + \mathbf{B}^G(\mathbf{x}, t) + \mathbf{B_J}(\mathbf{x}). \qquad (2.32)$$

The addition of this extra gradient field implies that during the time, $T_{\mathbf{J}}$, that current flows through the imaging object, an extra change of frequency occurs by $\Delta\omega = -\gamma|\mathbf{B_J}|$ which in turn changes the phase by $\Delta\phi = \gamma|\mathbf{B_J}|T_{\mathbf{J}} \approx \gamma B_{\mathbf{J}}^z T_{\mathbf{J}}$ yielding a new signal in k-space given by

$$S_{I_\pm}(\mathbf{k}) = \int_{\Omega_{z_0}} M_0(x,y,z_0)e^{i\phi_0}e^{i(\pm\gamma B_{\mathbf{J}}^z(x,y,z_0)T_{\mathbf{J}}+\delta(x,y,z_0))}e^{i(\mathbf{k}\cdot\mathbf{x})}d\mathbf{x}. \qquad (2.33)$$

Here, $\delta(x,y,z_0)$ is any systematic phase error of the MR machine, $\pm$ denotes the "positive/negative" direction of current through a pair of electrodes. From here we again notice that the signal is just the two dimensional Fourier transform of the transverse magnetization, $\mathbf{M}(x,y,z_0)$. By applying the 2D inverse Fourier transform, we arrive at two complex MR images

$$m_{I_\pm}(x,y,z_0) = M_0(x,y,z_0)e^{i\phi_0}e^{i(\pm\gamma B_{\mathbf{J}}^z(x,y,z_0)T_{\mathbf{J}}+\delta(x,y,z_0))}. \qquad (2.34)$$

From these two complex MR images it is needed to extract the incremental phase change which is defined as follows [WS08].

$$\Psi(x,y,z_0) = \arg\left(\frac{m_{I_+}(x,y,z_0)}{m_{I_-}(x,y,z_0)}\right) = 2\gamma T_{\mathbf{J}}\mathbf{B_J}(x,y,z_0). \qquad (2.35)$$

The $\arg(\cdot)$ operator thus includes any phase unwrapping algorithm. Afterwards, the magnetic field in the slice is given by

$$B_{\mathbf{J}}^z(x,y,z_0) = \frac{\Psi(x,y,z_0)}{2\gamma T_{\mathbf{J}}}. \qquad (2.36)$$

We note, from (2.35) that the systematic phase error from the MR machine is cancelled out by the use of two opposite currents, I_+ and I_- and that the phase is multiplied by 2 due to the application of the two currents.

When collecting multi slice data, it is essential both to collect the phase images and the magnitude images. The phase image holds the information on the $B_{\mathbf{J}}(x,y,z_0)$ and the magnitude images will hold information on the boundary geometry and location of the electrodes. This is because the MR magnitude image will be almost zero outside of the imaging object because of the lack of free protons. Furthermore, if the MR magnitude approaches zero inside the

imaging object, which could happen in gas filled organs, at the boundaries of the skeletal muscle or if a simple air bubble occurs, the measured $B_{\mathbf{J}}^z(x, y, z_0)$-data will be highly oscillatory due to the relation between the error in measured $B_{\mathbf{J}}^z(x, y, z_0)$-data and the MR magnitude given by[WS11]

$$s_{B_z} = \frac{1}{\sqrt{2}T_{\mathbf{J}}\mathbf{M}(x, y, z_0)}. \tag{2.37}$$

Where s_{B_z} is the standard deviation of measured $B_{\mathbf{J}}^z(x, y, z_0)$-data. Thus, if the MR magnitude becomes near zero, the standard deviation will go to infinity. Furthermore, we see that a longer time for the injection current will lower the standard deviation on measured $B_{\mathbf{J}}^z(x, y, z_0)$-data. We now have the necessary information to begin the next chapter concerning the forward problem of MREIT, where the goal is to be able to numerically generate data which could arise from a real life MREIT experiment. A typical sequence design for MREIT is shown in the next section together with a figure describing a single pulse sequence.

2.4.1   MREIT sequence design

Finally, we will shortly take the reader through a general rectangular sampling of k-space using MREIT. We will follow the application of a so-called spin-echo pulse sequence. Figure 2.3 shows a single pulse sequence for acquisition of a line of data in 2D k-space.
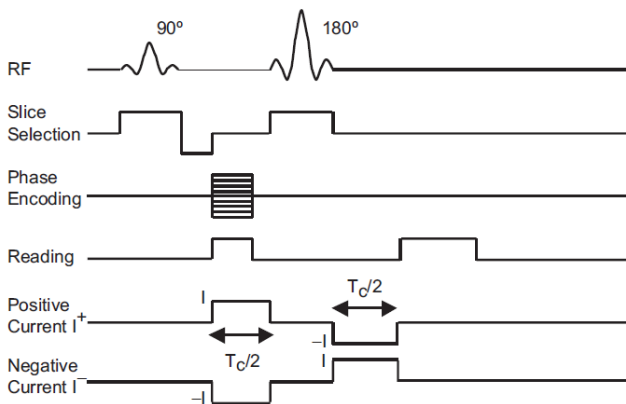
Figure 2.3: Typical spin echo pulse sequence applied in the setting of MREIT. Figure from [WS11]

As for MRI a magnetic field in the z-direction, where z-direction is parallel to the hull of the MR machine, is applied to magnetize the free protons of the body. A gradient field, $\mathbf{B}^{\mathbf{G}_z}(0, 0, \mathbf{G}^z \cdot \mathbf{x})$, is applied to choose the slice in the z-direction. Meanwhile the radio frequency field is applied, flipping the spinning protons 90 degrees for those protons for which the frequency condition, $\omega_1 = \omega(\mathbf{x})$ is upheld. This is only the case in the chosen slice. Thus, only flipping the magnetization in that slice by 90 degrees. Secondly, sequentially, the gradient fields $\mathbf{B}^{\mathbf{G}_y}(0, \mathbf{G}^y \cdot \mathbf{x}, 0)$ and $\mathbf{B}^{\mathbf{G}_x}(\mathbf{G}^x \cdot \mathbf{x}, 0, 0)$ is applied which moves the sampling space in a vertical- and a horizontal line through the positive quadrant of 2D k-space. Next, a new radio frequency field is applied, again while using the gradient field in the z-direction. This RF field flips the magnetization 180 degrees into the opposite quadrant of 2D k-space from where the real sampling starts while applying a gradient field in the x-direction. During both applications of $\mathbf{G}^x$ a positive or negative current is applied through a pair of electrodes. Thus sampling a full line of 2D k-space. A spin echo sequence is usually applied because after the initial flipping of the magnetization of 90 degrees some of the spinning protons will begin to de-phase. flipping the magnetization 180 degrees afterwards will result in de-phasing spins to re-phase and thus creating the so-called echo during which the re-phased sampling is taken, increasing the measurement signal. Repeating this procedure for new phase-encodings enables the machine to sample a rectangular grid of 2D k-space.

It is now time to address the mathematical rigour of the forward problem of known $\sigma \rightarrow B_z$. The following chapter will show the well posedness of the forward problem for two BVPs solving the same problem.

CHAPTER 3

The Forward Problem

In this chapter of the thesis, the forward problem of MREIT concerning the process of going from a known conductivity distribution, $\sigma(\mathbf{x})$ to the z-component of the magnetic field $\mathbf{B}$, i.e. B_z. Then from B_z to the complex k-space data which the MR machine measures.

We start by assuming a known conductivity distribution, $\sigma(\mathbf{x})$, for which certain assumption which the following section will go through applies, for $\mathbf{x} \in \Omega \subset \mathbb{R}^3$. We have seen from chapter 2 section 2.2 that given that a current flows through the domain, Ω, the governing equation for the potential distribution, $u = u(\mathbf{x})$ is

$$-\nabla \cdot (\sigma \nabla u) = 0, \text{ in } \Omega. \tag{3.1}$$

As described in the previous chapter, in MREIT electrodes are placed on the surface of the imaging object yielding boundary conditions associated with the hardware setup of the system. Two models of boundary conditions are investigated in the following sections of this chapter. One defined through the so-called Complete Electrode Model which assumes a current input through the wires, i.e. Neumann data and a single voltage measurement to gauge the solution and one setup consisting of a pure Robin boundary condition, i.e. using known equipotential distribution of voltage across the electrodes. The forward problem

then first consists of attaining the potential distribution across the domain. The two models are both investigated in terms of existence and uniqueness of this potential distribution solution. To do that, the Lax-Milgram lemma is applied which is stated in A.1. The two models are different ways of representing the same problem, i.e. finding the potential distribution. In literature, CEM is used most often when considering experiments related to EIT for instance in [JM10] and for that matter MREIT in [WS11]. This has to do with the practical matter of controlling the current being easier than controlling the potential across electrodes, however, the two models are in fact the same. This can be seen by examining the Dirichlet-to-Neumann operator given by

$$\Lambda_\sigma(g) = \sigma \frac{\partial u}{\partial \mathbf{n}}|_{\partial\Omega}, \tag{3.2}$$

where $g = u|_{\partial\Omega}$. The right hand side of (3.2) is the normal flux through the boundary which can be denoted by f, thus stating that the Dirichlet to Neumann map takes the form

$$\Lambda_\sigma \; : \; g \to f. \tag{3.3}$$

Generally for a potential distribution, $u \in H^1(\Omega)$, then $g \in H^{\frac{1}{2}}(\partial\Omega)$ is the trace of u A.8 and $f \in H^{-\frac{1}{2}}(\partial\Omega)$[DHK11]. (3.3) is a unique mapping [Uhl] with(under smoothness assumption on $\partial\Omega$) a well defined inverse mapping, the so-called Neumann-to-Dirichlet mapping which is given by

$$\Lambda_\sigma^{-1} \; : \; f \to g. \tag{3.4}$$

Under the criteria that $\int_{\partial\Omega} f \cdot \mathbf{n} \, dS = 0$, the Neumann to Dirichlet mapping is unique [Uhl]. Hence, there exists a unique pair, $(g, f) \in H^{\frac{1}{2}}(\partial\Omega) \times H^{-\frac{1}{2}}(\partial\Omega)$ for $u \in H^1(\Omega)$ solving (3.1). This in turn means that it does not matter whether the normal current component on the boundary is fixed or the voltages on the boundary is fixed when solving (3.1), it will still be the same problem. The two next sections of the thesis goes through first, the problem of knowing f and afterwards knowing g for solving the same problem.

3.1   The Two Models

The complete electrode model is a way to model electrode placements on the boundary, $\partial\Omega$ of a conducting media defined in the domain, Ω. A potential distribution in the Sobolev space $H^1(\Omega)$ and a set of constant potentials, $\{U_l\}_{l=1}^L$ on the electrodes, $\{e_l\}_{l=1}^L$, where $U = \{U_l\}_{l=1}^L \in \mathbb{R}^L$, the gathered solution, $(u(\mathbf{x}), U)$, resides in the sum of these spaces. I.e. $(u(\mathbf{x}), U) \in H^1(\Omega) \oplus \mathbb{R}^L$, and should satisfy the following boundary value problem for a known set of currents on the electrodes, $\{I_l\}_{l=1}^L$:

$$-\nabla \cdot \sigma(\mathbf{x})\nabla u(\mathbf{x}) = 0, \quad \text{in } \Omega, \tag{3.5}$$

$$\int_{e_1} \sigma(\mathbf{x})\frac{\partial u(\mathbf{x})}{\partial \mathbf{n}} \, dS = I_l, \quad l = 1..L, \tag{3.6}$$

$$\sigma(\mathbf{x})\frac{\partial u(\mathbf{x})}{\partial \mathbf{n}} = 0, \quad \text{on } \partial\Omega \backslash \cup_{l=1}^L e_l, \tag{3.7}$$

$$\alpha(\mathbf{x})u(\mathbf{x}) + z_l\sigma(\mathbf{x})\frac{\partial u(\mathbf{x})}{\partial \mathbf{n}} = U_l, \quad \text{on } e_l, \quad l = 1..L. \tag{3.8}$$

Here, Ω is the domain and $\partial\Omega$, the boundary containing the active electrodes. z_l is the contact impedance between electrode and skin. (3.5) is the general Poisson equation developed from Maxwell's equations in chapter 2. (3.6) is Kirchoff's law, stating that all current entering the conductor must also leave the conductor. (3.7) is the standard no flux Neumann BC stating that no energy leaves the system outside of the electrodes. (3.8) was developed and experimentally verified in [SCI92] for the complete electrode model, stating that the potential on each electrode must be equal to a constant while taking contact impedance into account. The Complete Electrode Model(CEM) also known as shunt-plus-surface-impedance model was created and tested for assigning a determined current pattern, $\{I_l\}_{l=1}^L$ and through this being able to predict a measurable potential pattern, $\{U_l\}_{l=1}^L$ on the same electrodes to within 0.1% which was the measurement accuracy [SCI92]. In this section, the assumptions of the model will be gone through, together with the proof of existence and uniqueness of the complete electrode model. Next, a model based on a Pure Robin boundary condition is presented.

$$-\nabla \cdot (\sigma(\mathbf{x})\nabla u(\mathbf{x})) = 0, \quad \text{in } \Omega, \tag{3.9}$$

$$\alpha(\mathbf{x})u(\mathbf{x}) + z_l\sigma(\mathbf{x})\frac{\partial u(\mathbf{x})}{\partial \mathbf{n}} = U_l, \quad \text{on } e_l, \quad l = 1..L. \tag{3.10}$$

The difference between CEM and Pure Robin is now that $\{U\}_{l=1}^{L}$ is known in the Pure Robin model, whereas they are only implicitly known to be piece-wise constant in CEM. To prove existence and uniqueness for the two models the Lax-Milgram lemma A.1 will be applied. However, first a description of the parameters in the two models must be given.

3.1.1   Assumptions on parameters for both models

This section will clarify the assumptions of the parameters which are present in the two models. First off the assumptions on the domain, Ω is gone through. It is assumed that Ω is a bounded domain in $\mathbb{R}^n$, $n = 3$, with a Lipschitz boundary denoted, $\partial\Omega$. The spatial coordinates are denoted by $\mathbf{x}$. The electrodes, denoted by e_l, where $2 \leq l \leq L$, $L \geq 2$, are assumed open connected subsets of $\partial\Omega$ and their closures are disjoint. From (3.5)-(3.10) it can be seen that some of the parameters are denoted by subscript "l". The assumptions described in this section are for the general case wherein all parameters are described as functions on either Ω or $\partial\Omega$.

The first parameter is the conductivity, σ, given, for $n = 3$ by

$$\sigma = \begin{bmatrix} \sigma_{11}(x) & \sigma_{12}(x) & \sigma_{13}(x) \\ \sigma_{21}(x) & \sigma_{22}(x) & \sigma_{23}(x) \\ \sigma_{31}(x) & \sigma_{32}(x) & \sigma_{33}(x) \end{bmatrix}, \tag{3.11}$$

Besides, the conductivity is assumed symmetric, i.e.

$$\sigma^{ij} = \sigma^{ji}. \tag{3.12}$$

Physiologically, this means that the conductivity is the same regardless of sign of the current running through the tissue. Furthermore, we have that the conductivity tensor is positive definite, meaning that

$$\xi^T \sigma(x)\xi \geq \theta_1 |\xi|^2 = c_1, \tag{3.13}$$

for almost everywhere $\mathbf{x} \in \Omega$ and all $\xi \in \mathbb{R}^3$, where the smallest eigenvalue of σ is larger than or equal to θ_1 [Eva10]. The same inequality can be stated using

the largest eigenvalue, creating an upper bound on σ.

$$\xi^T \sigma(x)\xi \leq \theta_2 |\xi|^2 = c_2, \tag{3.14}$$

for almost everywhere $\mathbf{x} \in \Omega$ and all $\xi \in \mathbb{R}^3$, where the largest eigenvalue of σ is smaller than or equal to θ_2.

These bounds are essential in the proof of linearity and the proof of coercivity which will follow in the next section. Thus, it is assumed that these eigenvalues exist.
Furthermore, the two assumptions (3.12) and (3.13) ensures that the partial differential operator, defining (3.5) and (3.9) is elliptic [Eva10]. Furthermore, formally, we assume that there exists a neighbourhood close to $\partial\Omega$ s.t. $\sigma \in C^1(\bar{\Omega} \cup U)$. Next, the function $z = z(x)$ is defined. Physically $z(x)$ represents the surface impedance and is bounded from below by a positive constant throughout the boundary, $\partial\Omega$. This requirement is essential to the following analysis. z is thus defined as

$$z(x) \geq c > 0 \text{ on } \partial\Omega, \quad c \in \mathbb{R}. \tag{3.15}$$

This definition of z allows the modelling of a certain extra resistance and thus, loss of energy, on the current when it passes from the domain and in to the electrode or the other way for that matter. The use of such a surface impedance has been experimentally verified in [SCI92].
Next we address the function, $\alpha = \alpha(x)$. α is a scaling parameter on u which aims to concatenate the two very different boundary conditions (3.7) and (3.8) in to one boundary condition, (3.10). α is thus defined as

$$\alpha(\mathbf{x}) = \begin{cases} 0 & \text{for} \quad \mathbf{x} \in \partial\Omega_1 \\ > c > 0 & \text{for} \quad \mathbf{x} \in \partial\Omega_2 \end{cases}, \quad c \in \mathbb{R}. \tag{3.16}$$

The function α then allows us to apply a Robin boundary condition on part of the boundary and implicitly employ a Neumann boundary condition on the rest of the surface if $\alpha = 0$. Hence, α is only non-zero on parts of $\partial\Omega$ where electrodes are applied.
Next, we define the function g which will contain the Dirichlet part of the Robin boundary condition, i.e. g contains our prescribed potentials, $\{U_l\}_{l=1}^L$ on $\partial\Omega$. g can in principle take any form. However, the boundary condition, (3.8) and (3.10) implies that g is piecewise constant on $\partial\Omega$. To be able to relate the two models and solve the same problem, g will be modelled as a function for the Pure

Robin model to emphasize the freedom of choice on this function-parameter for Pure Robin. Hence, g is given by:

$$g \; : \; \mathbf{x} \text{ on } \partial\Omega \rightarrow g(\mathbf{x}) \in \mathbb{R}. \tag{3.17}$$

If a non-trivial solution is to exist, then

$$\int_{\partial\Omega_1} g(\mathbf{x})dS \neq \int_{\partial\Omega_2} g(\mathbf{x})dS,$$

where subscripts 1 and 2 denote two different sets on the boundary with Lesbeque measure different from zero. g will not be specified as a function for CEM but only as the set of piece-wise constant functions, $\{U_l\}_{l=1}^L$ on $\partial\Omega$.

Lastly we define conditions on $\{I_l\}_{l=1}^L$ which is the known boundary data for CEM. There is but one condition on this set of parameters, namely:

$$\sum_{l=1}^L I_l = 0. \tag{3.18}$$

So far, the influence of electrode positioning has not been taken into account. This is mainly because it is not necessary to know these functions outside of the electrodes. The entire formulation of the boundary condition (3.10) and (3.8) can be reformulated by the use of the characteristic function, χ_l of the lth electrode by

$$\sigma\frac{\partial u}{\partial \mathbf{n}} = \sum_{l=1}^L \frac{1}{z}(g - \alpha u)\chi_l, \quad \text{ on } e_l. \tag{3.19}$$

Which allows for the use of $z(x)$,$g(x)$ and $\alpha(x)$ only on the electrodes. Since $u \in H^1(\Omega)$, and g being the trace of u, $g(x)$ must exist in the space $H^{\frac{1}{2}}(\partial\Omega)$. [AF03], [Theorem 7.39]. Finally, since the functions, $g(\mathbf{x})$,$z(\mathbf{x})$ and $\alpha(\mathbf{x})$ can all be expressed explicitly without the use of the characteristic function and loss of generality through the formulations given above and all three functions have shared Lesbegue measure $\neq 0$ on the electrodes, the formulation given by (3.10) will be used instead of (3.19) in the sections related to the Pure Robin model.

The formulation (3.19) is thus only stated to emphasize the general spaces in which these functions can exist. I.e. they are all traces of functions in $H^1(\Omega)$, and thus reside in $H^{\frac{1}{2}}(\partial\Omega)$.

3.1.2 Weak Formulation of CEM

To start with, assume that $(u, U) = (u(x), (U_l)_{l=1}^L) \in H^1(\Omega) \oplus \mathbb{R}^L$, and $H^1(\Omega) \oplus \mathbb{R}^L$ is henceforth known as H, is smooth enough such that we can multiply (3.5) by a test-function, $v \in H^1(\Omega)$ and integrate over the domain yielding

$$-\int_\Omega v \nabla \cdot (\sigma \nabla u) \, dx = 0.$$

Integration by parts yields

$$\int_\Omega v \nabla \cdot (\sigma \nabla u) \, dx = \int_{\partial\Omega} \sigma \frac{\partial u}{\partial \mathbf{n}} v \, dS - \int_\Omega \sigma \nabla u \cdot \nabla v \, dx = 0. \tag{3.20}$$

Now, (3.6) and (3.8) can be combined by the use of the characteristic function, χ_l, for each of the electrodes. This creates the BC

$$\sigma \frac{\partial u}{\partial \mathbf{n}} = \sum_{l=1}^L \frac{1}{z_l}(U_l - u)\chi_l \quad \text{on } e_l. \tag{3.21}$$

This equality holds in $H^{-\frac{1}{2}}(\partial\Omega)$, however, as $u \in H^1$, $U_l - u \in H^{\frac{1}{2}}(\partial\Omega)$. By the properties of Sobolev spaces[SCI92], this implies that $\sigma(\partial u/\partial \mathbf{n}) \in H^s$, $-\frac{1}{2} \le s < \frac{1}{2}$.

Insertion of (3.21) into (3.20) yields

$$\sum_{l=1}^L \frac{1}{z_l} \int_{e_l} (U_l - u)v \, dS - \int_\Omega (\sigma \nabla u) \cdot \nabla v \, dx = 0. \tag{3.22}$$

At the same time, we see from (3.7) and (3.8) that

$$\int_{e_l} u \ dS = \int_{e_l} \left(U_l - z_l \sigma \frac{\partial u}{\partial \mathbf{n}} \right) \ dS = U_l |e_l| - z_l I_l,$$

This in turn leads to for any set $\{V_l\}_{l=1}^{L}$

$$\sum_{l=1}^{L} \frac{1}{z_l} V_l \left(\int_{e_l} u \ dS - U_l |e_l| + z_l I_l \right) = 0. \qquad (3.23)$$

By adding (3.23) to (3.22), we get

$$\sum_{l=1}^{L} \frac{1}{z_l} \int_{e_l} (U_l - u) v \ dS - \int_{\Omega} (\sigma \nabla u) \cdot \nabla v \ dx + \sum_{l=1}^{L} \frac{1}{z_l} V_l \left(\int_{e_l} u \ dS - U_l |e_l| + z_l I_l \right) = 0 \Leftrightarrow$$

$$\sum_{l=1}^{L} \frac{1}{z_l} \int_{e_l} (U_l - u) v \ dS - \int_{\Omega} (\sigma \nabla u) \cdot \nabla v \ dx +$$

$$\sum_{l=1}^{L} \frac{1}{z_l} V_l \int_{e_l} u \ dS + \sum_{l=1}^{L} \frac{1}{z_l} V_l U_l |e_l| + \sum_{l=1}^{L} V_l I_l = 0 \Leftrightarrow$$

$$\sum_{l=1}^{L} \frac{1}{z_l} \int_{e_l} (U_l - u) v \ dS - \int_{\Omega} (\sigma \nabla u) \cdot \nabla v \ dx +$$

$$\sum_{l=1}^{L} \frac{1}{z_l} \int_{e_l} V_l u \ dS + \sum_{l=1}^{L} \frac{1}{z_l} \int_{e_l} V_l U_l \ dS + \sum_{l=1}^{L} V_l I_l = 0 \Leftrightarrow$$

$$\sum_{l=1}^{L} V_l I_l = \int_{\Omega} (\sigma \nabla u) \cdot \nabla v \ dx - \sum_{l=1}^{L} \frac{1}{z_l} \int_{e_l} (U_l v - uv + V_l u - U_l V_l) \ dS \Leftrightarrow$$

$$\sum_{l=1}^{L} V_l I_l = \int_{\Omega} (\sigma \nabla u) \cdot \nabla v \ dx + \sum_{l=1}^{L} \frac{1}{z_l} \int_{e_l} (u - U_l) (v - V_l) \ dS.$$

Now, by defining the right hand side as the bilinear mapping $a : H \times H \to \mathbb{R}$ through

$$a((u, U), (v, V)) = \int_{\Omega} (\sigma \nabla u) \cdot \nabla v \ dx + \sum_{l=1}^{L} \frac{1}{z_l} \int_{e_l} (u - U_l)(v - V_l) \ dS, \qquad (3.24)$$

we get

$$a((u, U), (v, V)) = \sum_{l=1}^{L} I_l V_l. \tag{3.25}$$

We require that the above be satisfied $\forall (v, V) \in H$.

This mapping (3.24) was found by the assumption that (u, U) satisfied (3.5)-(3.8). It should also be shown that given $(u, U) \in H$ satisfying (3.25), then (3.5)-(3.8) is satisfied. The latter is verified by choosing different sets (v, V) and thus, acquiring (3.5)-(3.8). Details on this can be seen in [SCI92].

3.1.3 Existence and uniqueness for CEM

Existence and uniqueness now follows from Lax-Milgram's lemma. However, the current bilinear mapping, (3.25) does not satisfy (A.2) because when computing

$$a((u, U), (u, U)) = \int_{\Omega} (\sigma \nabla u) \cdot \nabla u \, dx + \sum_{l=1}^{L} \int_{e_l} |u - U_l|^2 \, dS. \tag{3.26}$$

Setting $a((u, U), (u, U)) = 0$ does not imply that $u = 0$ but only that $u = U_1 = \ldots = U_L = \texttt{const}$. Therefore, the quotient space, $\dot{H} = H/\mathbb{R}$ is introduced, where the elements $(u, U) \in H$ and $(v, V) \in H$ are equivalent if $u - v = U_1 - V_1 = \ldots = U_L - V_L = \texttt{const}$. This quotient space is equipped with the usual quotient norm on the space, H which, as stated, is given by the direct sum of $H^1(\Omega)$ and $\mathbb{R}^L$. Thus,

$$\|(u, U)\|_{\dot{H}} = \inf_{c \in \mathbb{R}} (\|u - c\|_{H^1(\Omega)}^2 + \|U - c\|_{\mathbb{R}^L}^2)^{\frac{1}{2}}. \tag{3.27}$$

However, proving the conditions of Lax-Milgram's lemma is easier using the equivalent norm(see Appendix B for equivalence proof)

$$\|(u, U)\|_{\star} = \left(\|\nabla u\|_{L^2(\Omega)}^2 + \sum_{l=1}^{L} \int_{e_l} |u(x) - U_l|^2 \, dS \right)^{\frac{1}{2}}. \tag{3.28}$$

The definition of equivalence of norms is given by

$$\lambda \|(u,U)\|_\star \leq \|(u,U)\|_{\dot{H}} \leq \Lambda \|(u,U)\|_\star, \ \ \lambda < \Lambda \in \mathbb{R}^+. \tag{3.29}$$

Thus, since the equivalence is proven in Appendix B, we can set up a bound as following

$$C\|(u,U)\|_\star^2 \geq \|(u,U)\|_{\dot{H}}^2. \tag{3.30}$$

Hence, we just need to show that the bilinear mapping, $a((u,U),(u,U))$ can be formulated through $\|\cdot\|_\star$. This happens straight forward by using the ellipticity of σ (3.13):

$$a((u,U),(u,U)) = \int_\Omega (\sigma \nabla u) \cdot \nabla u \ dx + \sum_{l=1}^{L} \int_{e_l} |u - U_l|^2 \ dS \tag{3.31}$$

$$\geq c_1 \int_\Omega |\nabla u|^2 \ dx + \sum_{l=1}^{L} \int_{e_l} |u - U_l|^2 \ dS. \tag{3.32}$$

$$= c_1 \|\nabla u\|_{L^2(\Omega)}^2 + \sum_{l=1}^{L} \int_{e_l} |u - U_l|^2 \ dS. \tag{3.33}$$

$$= C_1 \|(u,U)\|_\star^2. \tag{3.34}$$

Hence, $a((u,U),(u,U)) \geq C_1\|(u,U)\|_\star \geq C_2\|(u,U)\|_{\dot{H}}$ and is thus bounded from below by a strictly positive constant, i.e. (A.2) is shown. It remains to show that $|a((u,U),(v,V))|$ is bounded from above. It will prove favourable to square the expression $a((u,U),(v,V))$ before starting the calculations. Furthermore, the $\|\cdot\|_\star$-norm will be applied, abusing the equivalence with $\|\cdot\|_{\dot{H}}$. This means that it will have to be proven that

$$a((u,U),(v,V))^2 \leq C\|(u,U)\|_{\dot{H}}^2 \|(v,V)\|_{\dot{H}}^2 \leq C\|(u,U)\|_\star^2 \|(v,V)\|_\star^2. \tag{3.35}$$

We start by writing out the definition and apply standard inequalities:

$$|a((u, U), (v, V))|^2 = \left(\int_\Omega (\sigma \nabla u) \cdot \nabla v \, dx + \sum_{l=1}^L \frac{1}{z_l} \int_{e_l} (u - U_l)(v - V_l) \, dS \right)^2$$

$$\leq \left(c_2 \int_\Omega (\sigma \nabla u) \cdot \nabla v \, dx + \sum_{l=1}^L \inf_{z_l \in \{z_l\}_{l=1}^L} \frac{1}{z_l} \int_{e_l} (u - U_l)(v - V_l) dS \right)^2.$$

Here we have applied the ellipticity of σ (3.14) and the boundedness of $\frac{1}{z_l}$. Next we apply Cauchy-Schwartz inequality and expand the square through $(a+b)^2 = a^2 + b^2 + 2ab$.

$$|a((u, U), (v, V))|^2$$

$$\leq \left(C_1 \|\nabla u\|_{L^2(\Omega)} \|\nabla v\|_{L^2(\Omega)} + C_2 \sum_{l=1}^L \int_{e_l} (u - U_l)(v - V_l) dS \right)^2$$

$$\leq C_1^2 \|\nabla u\|_{L^2(\Omega)}^2 \|\nabla v\|_{L^2(\Omega)}^2 + C_2 \sum_{l=1}^L \int_{e_l} (u - U_l)^2 (v - V_l)^2 dS +$$

$$2 C_1 C_2 \|\nabla u\|_{L^2(\Omega)} \|\nabla v\|_{L^2(\Omega)} \sum_{l=1}^L \int_{e_l} (u - U_l)(v - V_l) dS$$

$$\leq C(\|\nabla u\|_{L^2(\Omega)}^2 \|\nabla v\|_{L^2(\Omega)}^2 + \sum_{l=1}^L \int_{e_l} (u - U_l)^2 (v - V_l)^2 dS +$$

$$2 \|\nabla u\|_{L^2(\Omega)} \|\nabla v\|_{L^2(\Omega)} \sum_{l=1}^L \int_{e_l} (u - U_l)(v - V_l) dS).$$

From here we identify

$$a = \|\nabla u\| \sum_{l=1}^L \int_{e_l} |v - V_l| dS, \tag{3.36}$$

$$b = \|\nabla v\| \sum_{l=1}^L \int_{e_l} |u - U_l| dS. \tag{3.37}$$

Next we take a look at the product, $\|(u, U)\|_\star^2 \|(v, V)\|_\star^2$ which becomes

$$\|(u,U)\|_\star^2 \|(v,V)\|_\star^2$$

$$= \left(\|\nabla u\|_{L^2(\Omega)}^2 + \sum_{l=1}^{L} \int_{e_l} (u-U_l)^2 dS \right) \left(\|\nabla v\|_{L^2(\Omega)}^2 + \sum_{l=1}^{L} \int_{e_l} (v-V_l)^2 dS \right)$$

$$= \|\nabla u\|_{L^2(\Omega)}^2 \|\nabla v\|_{L^2(\Omega)}^2 + \sum_{l=1}^{L} \int_{e_l} (u-U_l)^2 (v-V_l)^2 dS +$$

$$\|\nabla u\|_{L^2(\Omega)}^2 \sum_{l=1}^{L} \int_{e_l} (v-V_l)^2 dS + \|\nabla v\|_{L^2(\Omega)}^2 \sum_{l=1}^{L} \int_{e_l} (u-U_l)^2 dS$$

Now, we can identify the two terms in both derivations as being the same. Then we can apply the inequality $2ab \le a^2 + b^2$ when a and b are defined through (3.36) and (3.37), then we obtain the inequality.

$$a((u,U),(v,V))^2 \le C_1 \|(u,U)\|_\star^2 \|(v,V)\|_\star^2 \Leftrightarrow$$
$$|a((u,U),(v,V))| \le C_2 \|(u,U)\|_{\dot H} \|(v,V)\|_{\dot H}.$$

Thus, the boundedness of $a(\cdot,\cdot)$ has been shown. It is now possible to apply Lax-Milgram's lemma to show existence and uniqueness to the complete electrode model.

It is now needed to show that the linear mapping

$$f : (v,V) \to \sum_{l=1}^{L} I_l V_l$$

is well defined and continuous. if $(v,V) \sim (\tilde v, \tilde V)$ then due to (3.6)

$$f(v,V) = \sum_{l=1}^{L} I_l V_l = \sum_{i=1}^{L} I_l (V_l - \text{const}) = \sum_{i=1}^{L} I_l \tilde V_l = f(\tilde v, \tilde V).$$

And, for $c \in \mathbb{R}$, a constant with

$$(\|v - c\|_{H^1(\Omega)}^2 + \|V - c\|_{\mathcal{C}^L}^2)^{\frac{1}{2}} \le \|(v,V)\| + \epsilon,$$

then

$$|f(v,V)| = |\sum_{l=1}^{L} I_l(V_l - c)| \le \|I\|_{\mathbb{R}^L} \|V - c\|_{\mathbb{R}^L} \le \|I\|_{\mathbb{R}^L} (\|(v,V)\| + \epsilon),$$

yields continuity. Now the complete electrode model has a unique solution in the space $\dot{H}$, however, since this space is a quotient space, it is still necessary to choose one solution from the infinity of similar solutions that a quotient space allows. Hence, the ground potential gauge is chosen by restricting the potential pattern, $\{U_l\}_{l=1}^{L}$ as following:

$$\sum_{l=1}^{L} U_l = 0, \tag{3.38}$$

Then the complete electrode model finds a unique solution to the unknown potential distribution $u(\mathbf{x})$. This can be formulated in a theorem concatenating all the assumptions of the parameters.

THEOREM 3.1 *Let a boundary value problem be given by* (3.5)-(3.8) *on a domain* $\Omega \in \mathbb{R}^3$ *with a Lipschitz boundary,* $\partial\Omega$. *Then for* σ *defined through* (3.12)- (3.14), z *defined by* (3.15), α *defined by* (3.16), $\{I_l\}_{l=1}^{L}$ *defined by* (3.18) *and* $\{U_l\}_{l=1}^{L} \in \mathbb{R}^L$ *satisfying* (3.38), *there exists a unique* $(u, U) \in \dot{H}(\Omega)$ *satisfying* (3.25), $\forall(v, V) \in \dot{H}(\Omega)$.

The complete electrode model thus makes it possible to define Neumann boundary conditions through a current pattern, $\{I_l\}_{l=1}^{L}$ satisfying Kirchoff's law and always obtain a unique solution for the potential, $u(\mathbf{x})$. And furthermore, the model predicts the associated potential pattern on the same electrodes, $\{U_l\}_{l=1}^{L}$ within measuring error of 0.1% [SCI92]. The next section involves the complement scenario, i.e. given some known potential pattern $\{U_l\}_{l=1}^{L}$ find a unique solution to the potential, $u(\mathbf{x})$.

3.1.4 Weak formulation of Pure Robin model

This section aims to provide the bilinear form which is needed to prove existence and uniqueness of such a solution and relies on the Lax-Milgram lemma. Assume a solution u sufficiently smooth, i.e. $u \in H^1$, then we can multiply (3.9) by a test function, $v \in H^1$ and integrate over the domain, yielding

$$-\int_{\Omega} \nabla \cdot (\sigma \nabla u)v \, dx = 0. \tag{3.39}$$

Then, as usual by applying integration by parts and remembering the anisotropic definition of σ, we arrive at

$$\int_{\Omega} (\sigma \nabla u) \cdot \nabla v \, dx - \int_{\partial \Omega} \sigma \frac{\partial u}{\partial \mathbf{n}} v \, dS = 0. \qquad (3.40)$$

Now, by rearranging (3.10) we get

$$\sigma \frac{\partial u}{\partial \mathbf{n}} = \frac{1}{z} \left(g - \alpha u \right). \qquad (3.41)$$

Inserting (3.41) into (3.40) we arrive at

$$\int_{\Omega} (\sigma \nabla u) \cdot \nabla v \, dx - \int_{\partial \Omega} \left(\frac{1}{z} \left(g - \alpha u \right) \right) v \, dS = 0 \Leftrightarrow \qquad (3.42)$$

$$\int_{\Omega} (\sigma \nabla u) \cdot \nabla v \, dx - \int_{\partial \Omega} \left(\frac{1}{z} g v - \frac{1}{z} \alpha u v \, dS \right) = 0 \Leftrightarrow \qquad (3.43)$$

$$\int_{\Omega} (\sigma \nabla u) \cdot \nabla v \, dx + \int_{\partial \Omega} \frac{1}{z} \alpha u v \, dS = \int_{\partial \Omega} \frac{1}{z} g v \, dS. \qquad (3.44)$$

We then require that the variational form (3.44) be satisfied for all $v \in H^1$ for u to satisfy (3.9) and (3.10). Now, by defining the left hand side as $a(u, v) = \int_{\Omega} (\sigma \nabla u) \cdot \nabla v \, dx + \int_{\partial \Omega} \frac{1}{z} \alpha u v \, dS$ and the right hand side as $L(v) = \int_{\partial \Omega} \frac{1}{z} g v \, dS$. we have arrived at a bilinear form, $a(u, v) = L(v)$.

3.1.5 Boundedness

Now, let us check the conditions of Lax-Milgram's lemma. First we check (A.1):

This is done by expressing the term $|a(u, v)|$ and move the absolutes on the two terms on the right hand side.

$$|a(u, v)| = \left| \int_{\Omega} (\sigma \nabla u) \cdot \nabla v \, dx + \int_{\partial \Omega} \frac{1}{z} \alpha u v \, dS \right| \qquad (3.45)$$

$$\leq \left| \int_{\Omega} (\sigma \nabla u) \cdot \nabla v \, dx \right| + \left| \int_{\partial \Omega} \frac{1}{z} \alpha u v \, dS \right|. \qquad (3.46)$$

We now move the absolutes into the integral and apply the bound from (3.14) yielding

$$|a(u,v)| \leq \int_{\Omega} |(\sigma \nabla u) \cdot \nabla v| \ dx + \left| \int_{\partial \Omega} \frac{1}{z} \alpha uv \ dS \right|$$

$$\leq \int_{\Omega} c_2 \, |\nabla u \cdot \nabla v| \ dx + \left| \int_{\partial \Omega} \frac{1}{z} \alpha uv \ dS \right|$$

$$= c_2 \int_{\Omega} |\nabla u \cdot \nabla v| \ dx + \left| \int_{\partial \Omega} \frac{1}{z} \alpha uv \ dS \right|.$$

Then we employ Cauchy-Schwartz' inequality to the first term yielding

$$|a(u,v)| \leq c_2 \left(\int_{\Omega} |\nabla u|^2 \ dx \right)^{\frac{1}{2}} \left(\int_{\Omega} |\nabla v|^2 \ dx \right)^{\frac{1}{2}} + \left| \int_{\partial \Omega} \frac{1}{z} \alpha uv \ dS \right|.$$

We now use that $\|\nabla u\|_{L^2(\Omega)} = \left(\int_{\Omega} |\nabla u|^2 \ dx \right)^{\frac{1}{2}} \leq \|u\|_{H^1(\Omega)} = \left(\int_{\Omega} u^2 + |\nabla u|^2 \ dx \right)^{\frac{1}{2}}$, to simplify the above expression in terms of norms in the Sobolev space, $H^1(\Omega)$.

$$|a(u,v)| \leq c_2 \|u\|_{H^1(\Omega)} \|v\|_{H^1(\Omega)} + \left| \int_{\partial \Omega} \frac{1}{z} \alpha uv \ dS \right|.$$

We now turn to the boundary expression. Again we see an inner product in the form of $(\frac{1}{z} \alpha u, v)$. $z(x)$ and $\alpha(x)$ are both known functions which were defined earlier and their product can be considered in the usual sense and thus, has a well defined maximum given by

$$\beta_{\alpha,z} = \sup_{x \in \partial \Omega} \{ x \ : \ \frac{1}{z(x)} \alpha(x) \}. \tag{3.47}$$

Using this maximum we can obtain a bound for the boundary term.

$$|a(u,v)| \leq c_2 \|u\|_{H^1(\Omega)} \|v\|_{H^1(\Omega)} + \left| \int_{\partial \Omega} \frac{1}{z} \alpha uv \ dS \right|$$

$$\leq c_2 \|u\|_{H^1(\Omega)} \|v\|_{H^1(\Omega)} + \int_{\partial \Omega} \beta_{\alpha,z} \, |uv| \ dS.$$

Now, by moving the constant outside, we end up in the form of

$$|a(u,v)| \leq c_2 \|u\|_{H^1(\Omega)} \|v\|_{H^1(\Omega)} + \beta_{\alpha,z} \int_{\partial\Omega} |uv| \ dS.$$

We then again apply Cauchy-Schwartz' inequality resulting in

$$|a(u,v)| \leq c_2 \|u\|_{H^1(\Omega)} \|v\|_{H^1(\Omega)} + \beta_{\alpha,z} \left(\int_{\partial\Omega} |u|^2 \ dS \right)^{\frac{1}{2}} \left(\int_{\partial\Omega} |v|^2 \ dS \right)^{\frac{1}{2}}.$$

This in turn leads to the definition of the norm in $L^2(\partial\Omega)$

$$|a(u,v)| \leq c_2 \|u\|_{H^1(\Omega)} \|v\|_{H^1(\Omega)} + \beta_{\alpha,z} \|u\|_{L^2(\partial\Omega)} \|v\|_{L^2(\partial\Omega)}. \tag{3.48}$$

Now, by applying the trace theorem (A.8), we can convert the expressions of the L^2 norm on the boundary to expression of the norm in the Sobolev space, H^1, on the domain, Ω.

$$|a(u,v)| \leq c_2 \|u\|_{H^1(\Omega)} \|v\|_{H^1(\Omega)} + \beta_{\alpha,z} c_3 \|u\|_{H^1(\Omega)} \|v\|_{H^1(\Omega)}. \tag{3.49}$$

And finally by rearranging the terms and gathering constants, we have an expression of the form

$$|a(u,v)| \leq (c_2 + \beta_{\alpha,z} c_3) \|u\|_{H^1(\Omega)} \|v\|_{H^1(\Omega)} \tag{3.50}$$

$$= \gamma \|u\|_{H^1(\Omega)} \|v\|_{H^1(\Omega)}. \tag{3.51}$$

3.1.6 Coercivity

It is then time to show the coercivity of $a(u,v)$ (A.2). This is done by proof of contradiction and the use of the compactness of Hilbert-spaces. First, assume that $a(u,v)$ is not coercive then there exists a sequence $\{w_n\} \subset H^1$ such that

$$\|w_n\|_{H^1(\Omega)} = 1 \ \text{ and } \ a(w_n, w_n) \to 0, \tag{3.52}$$

as $\{w_n\}$ is a bounded sequence in a Hilbert space, $H^1(\Omega)$, then there exists a weakly convergent subsequence, which for simplicity is also denoted, $\{w_n\} \rightharpoonup w \in H^1(\Omega)$. Since $\partial\Omega$ is assumed to be Lipschitz, $H^1(\Omega)$ is compactly embedded in $L^2(\Omega)$, i.e. $H^1(\Omega) \hookrightarrow L^2(\Omega)$, then $w_n \to w$ in $L^2(\Omega)$ and $\nabla w_n \rightharpoonup \nabla w$ in $L^2(\Omega; \mathbb{R}^3)$.

Now, by definition of the assumption and the use of ellipticity of σ, (3.13) we obtain,

$$a(w_n, w_n) = \int_\Omega (\sigma \nabla w_n) \cdot \nabla w_n \; dx + \int_{\partial\Omega} \frac{1}{z} \alpha w_n w_n \; dS \to 0, \Leftrightarrow \quad (3.53)$$

$$a(w_n, w_n) \geq \int_\Omega c_2 |\nabla w_n|^2 \; dx + \int_{\partial\Omega} \frac{1}{z} \alpha w_n^2 \; dS \to 0. \quad (3.54)$$

This leads to

$$\int_\Omega |\nabla w_n|^2 \; dx \to 0. \quad (3.55)$$

Together with this, the weak convergence inequality [wea13] shows that

$$\int_\Omega |\nabla w|^2 \; dx \leq \liminf_{n\to\infty} \int_\Omega |\nabla w_n|^2 \; dx = 0. \quad (3.56)$$

thus, w is constant. We also see from the assumption that

$$\int_\Omega w^2 \; dx = \lim_{n\to\infty} \int_\Omega w_n^2 \; dx = 1. \quad (3.57)$$

However, we also have that $w_n \to w$ in $L^2(\partial\Omega)$, and $\frac{1}{z}\alpha > 0$ from (3.54) and (3.55) that

$$\int_{\partial\Omega} w^2 \; dS = \lim_{n\to\infty} \int_{\partial\Omega} w_n^2 \; dS = 0. \quad (3.58)$$

We see from (3.58) that $w = 0$ on $\partial\Omega$ and that this is a contradiction to (3.57) if $w \in H^1(\Omega)$. Thus, there does not exist a sequence satisfying (3.52). Hence, the negation of the statement is:
For all sequences in $H^1(\Omega)$, $\|w_n\|_{H^1(\Omega)} = 1$, $a(w_n, w_n)$ is bounded from below by a strictly positive constant, $\delta > 0$. This goes for all functions, $w \in H^1(\Omega)$ as we, through the completeness of the Hilbert space, can always find a weakly convergent subsequence $w_n \rightharpoonup w$. Thus, $a(w, w) \geq \delta \|w\|^2$ and is coercive.
Lastly, before applying Lax-Milgram, we need to show that $L(v)$ is bounded and

linear. As with $\frac{1}{z}\alpha$ from the continuity proof of $a(u,v)$ we need to establish a bound on the product of $\frac{1}{z}g$. This bound, done in the same way as for $\frac{1}{z}\alpha$ will be called β.

$$|L(v)| = \left| \int_{\partial\Omega} \frac{1}{z} gv \, dS \right| \tag{3.59}$$

$$\leq \beta \int_{\partial\Omega} |v| \, dS \tag{3.60}$$

$$\leq \beta \|v\|_{L^2(\partial\Omega)} \tag{3.61}$$

By the trace theorem (A.8)

$$|L(v)| \leq \beta \|v\|_{L^2(\partial\Omega)} \tag{3.62}$$

$$\leq c\beta \|v\|_{H^1(\Omega)} \tag{3.63}$$

$$\leq c_2 \|v\|_{H^1(\Omega)}. \tag{3.64}$$

Thus, $L(\cdot)$ is bounded and obviously linear.

It is now time to apply Lax-Milgram's lemma to prove existence and uniqueness for a solution to the PDE given by (3.9) and (3.10). It has, in the previous section been shown that we can find constants, γ and δ such that (A.1) and (A.2) is upheld. Then, as $L(v)$ is a continuous, bounded, linear operator, there exists a unique $u \in H^1(\Omega)$ s.t. $a(u,v) = L(v)$. Furthermore, a note on the boundary, $\partial\Omega$ is needed. It is strictly only in the proof of coerciveness of $a(u,v)$ that it was mentioned that $\partial\Omega$ is assumed Lipschitz. Generally speaking, the proof of continuity falls apart, if $\partial\Omega$ is not Lipschitz, since the Trace theorem relies heavily on this assumption. The above statement can be compressed into a theorem:

THEOREM 3.2 *Let a boundary value problem be given by (3.9)-(3.10) on a domain $\Omega \in \mathbb{R}^3$ with a Lipschitz boundary, $\partial\Omega$. Then for σ defined through (3.12)-(3.14), z defined by (3.15), α defined by (3.16), g defined by (3.17), there exists a unique $u \in H^1(\Omega)$ satisfying (3.44), $\forall v \in H^1(\Omega)$.*

Furthermore, given further restriction on g to coincide with the piece-wise constant definition of $\{U_l\}_{l=1}^L$ from CEM, a corollary can take form of:

COROLLARY 3.3 *Iff $g = \{U_l\}_{l=1}^L$ from 3.1, then the unique solution $u \in H^1(\Omega)$ of 3.2 is the same unique solution as $(u,U) \in \dot{H}$ from 3.1*

3.2   Model Comparison

This section will compare the numerical solution of the two models and test
the corollary given above. For the solution to be physically accurate in a no-
sink/source setup. As mentioned earlier, the complete electrode model which
finds a solution in the quotient space, $\dot{H}$, must then have chosen a gauge on
the potential. In this case the ground-potential gauge is chosen. To compare
the models, this gauge is also chosen for the model provided by the pure robin
bc model, however, it should be noted that this is not a necessary condition for
a unique solution. Thus, the potentials on all the electrodes, $\{e_l\}_{l=1}^{L}$, for the
Robin bc model must also satisfy the condition

$$\sum_{l=1}^{L} U_l = \sum_{l=1}^{L} g(\mathbf{x})\chi_l = 0. \qquad (3.65)$$

With χ_l being the characteristic function for the l'th electrode. The two models
are implemented in Python using FEniCS[LMea12]. First of all the two models
rely on two different types of boundary conditions which has been discussed
before. To make sure that the same potentials on the boundary is used the two
models are run in series and the potentials found through CEM is then applied
as the boundary condition for the Pure Robin bc model. For testing, a piecewise
constant isotropic conductivity is used and can be seen in figure 3.1.
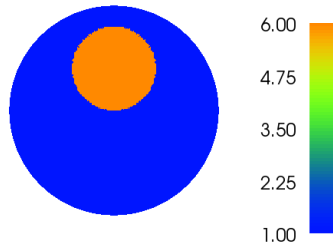

Figure 3.1: conductivity distribution, $\sigma(\mathbf{x})$. An inner sub-
domain with a $\sigma = 6$ inside the unit circle with
$\sigma = 1$.

For the model comparison, four electrodes are placed on the surface satisfying
the condition (**??**). Assuming that the electrodes are made of the same material
and attached to the same biological material, the set of surface impedances,

$\{z_l\}_{l=1}^{L}$ are all equal and set to 0.8. The two solutions for the potential, $u(\mathbf{x})$, is shown in figure 3.2

(a) Solution, $u(\mathbf{x})$, from CEM, mesh size   (b) Solution, $u(\mathbf{x})$, from Pure Robin
      of 102400 triangles   Model, mesh size of 102400 triangles
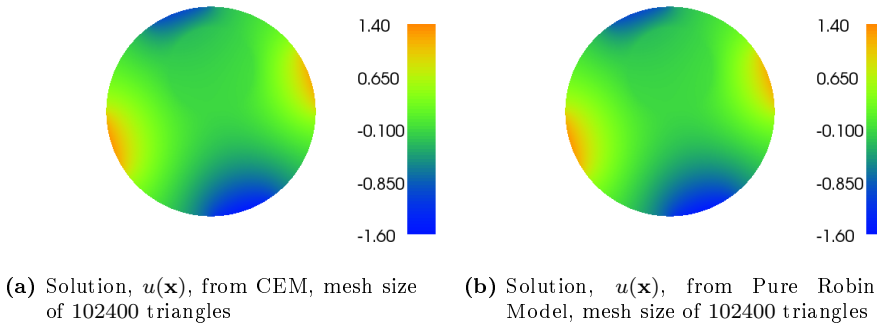
Figure 3.2

Visually, the two solutions looks very much alike and this observation can be seen by plot of the difference between the two solutions, seen in figure 3.3
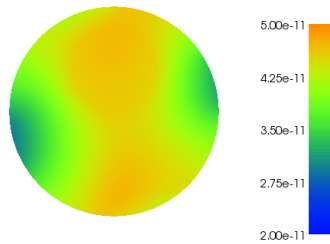
Figure 3.3: Difference between the solution for the potential
                    from the two different models, i.e. $u_{CEM}(\mathbf{x}) -$
                    $u_{Rob}(\mathbf{x})$, mesh size of 102400 triangles

From 3.3 it can be seen that the difference between the two solutions are in the order of $1e-11$ at most and through further testing this difference is invariant to mesh-size. Thus, we can conclude that the two solution strategies for finding the potential distribution, $u(\mathbf{x})$, result in the same unique solution if disregarding numerical errors. Furthermore, when computing the flux(current), $-\sigma \nabla u$. The same order of difference between the solutions can be observed.
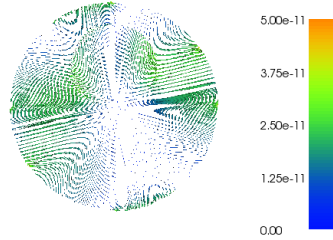
Figure 3.4: Difference between the solution for the current, $-\sigma\nabla u$, from the two different models, i.e. $u_{CEM}(\mathbf{x}) - u_{Rob}(\mathbf{x})$, mesh size of 102400 triangles

Because the current distribution is actually the distribution of interest in the context of MREIT, showing that the two solution strategies correspond to the same solution for the current distribution within measurable accuracy is an important feature. In the end of this comparison, the solution time given the two models is shown together with mesh size.

| number of elements	19600	40000	67600	102400
CEM solution time(s)	11.7	66.5	215.3	523.8
Robin solution time(s)	0.7	1.5	2.9	4.7

Table 3.1: Solution time for the two models

From table 3.1 it can be seen that the solution time using the CEM grows much faster than when using the Robin bc model. This can be shown as well, in a log-log plot of the number of elements versus the solution time seen in figure 3.5.
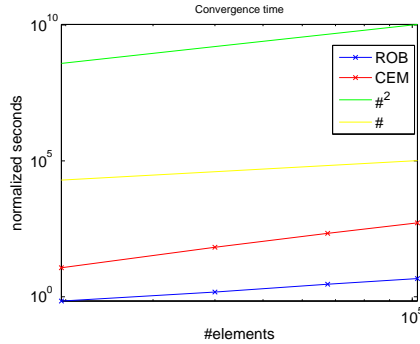
Figure 3.5: log-log plot of number of elements in the mesh versus convergence time for the two models together with $\#elements^2$ and $\#elements$ For isotropic conductivity

From figure 3.5 it can be seen that the Robin solution model follows a solution time which is close to a scaling of the number of elements, however a little slower, i.e. $SOL_{t,ROB} \sim \#elements^{)1;2(}$ and it can also be observed that the CEM exhibits a solution time which is much slower, i.e. $SOL_{t,CEM} \sim \#elements^{)2;3(}$. visually it seems like there is approximately one order of convergence rate between the two models. The two models are implemented in a very similar manner. The reason that the CEM model takes so much longer to solve for the potential is that the solution must be found in the mixed function space of $H^1(\Omega) \oplus \mathbb{R}^L$. This function space requires a much larger linear system of equations to solve for. The full set of plots for the four different mesh sizes can be seen in Appendix C together with individual current distributions for each solution. In figure 3.6 we see the same plot of convergence time for the two solution models with more data points. This time, an anisotropic conductivity distribution is applied.
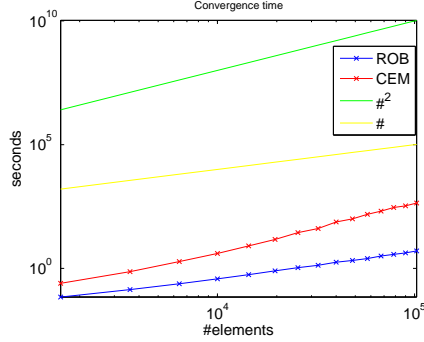
Figure 3.6: log-log plot of number of elements in the mesh versus convergence time for the two models together with $\#elements^2$ and $\#elements$. For anisotropic conductivity

It can be seen that the relationship between computational time and for each of the models and grid-size is not affected by applying an anisotropic conductivity distribution. The next section concerns how to go from a known $\mathbf{J} = -\sigma(\mathbf{x})\nabla u(\mathbf{x})$ to the magnetic flux density, $\mathbf{B}_z(\mathbf{x})$.

3.3   Computing B_z

The internal B data can be computed through the Biot-Savart law given below. The computation neglects the influence of external wires and introduces the position vector $\mathbf{r} = (x, y, z)$ to ease notation because the individual coordinates are needed.

$$B(\mathbf{r}) = \frac{\mu_0}{4\pi} \int_\Omega -\sigma(\mathbf{r}')\nabla u(\mathbf{r}') \times \frac{\mathbf{r} - \mathbf{r}'}{|\mathbf{r} - \mathbf{r}'|^3} \, d\mathbf{r}' + H(\mathbf{r}) \qquad (3.66)$$

Here, $\mathbf{x} \in \mathbb{R}^3$. Thus, the computation of the internally generated magnetic field is a sum of contributions of all infitisimal parts of the object, $\Omega \in \mathbb{R}^3$. $\mathbf{e}_z = (0, 0, 1)$, extracts the z-component of the Biot-Savart Law for the relation between the current density in a conductor and the magnetic field. $\sigma(\mathbf{r})$ is the known conductivity and $H(\mathbf{x})$ is a harmonic function describing the contribution to the internal magnetic field from external wires. One aims to minimize the effect of $H(\mathbf{x})$ in any inverse problem and is thus neglected in any further computations.

3.3.1   Single Slice Calculation

This small section aims to prove that handling the above computation in the entire space, $\Omega \in \mathbb{R}^3$, under certain assumptions can be handled as a computation in $\Omega_{z_0} \in \mathbb{R}^2$. The assumptions needed for this proof is that $\sigma(x, y, z_1) = \sigma(x, y, z_2)$, $\forall z_1, z_2$. and that boundary conditions apply throughout the entire infinite z-axis. We thus consider an infinite cylinder with equally varying conductivity distribution in all of z. The assumption of the infinite cylinder has some merit to the application of the human body. Many body parts are locally cylindrical.

PROPOSITION 3.4 *Given a cylinder with non-varying conductivity distribution, $\sigma(x, y, z)$ and current distribution, $J(x, y, z)$ along the z-axis, the expression for $B_z(x, y, z_0)$ given by (3.66) can be reduced to a 2-dimensional integral over the plane, (x, y, z_0) and a single integral over the volume (x, y, z).*

PROOF. It will be shown that a contribution from a point $(x_1, y_1, z + \epsilon)$ is the same but opposite of a contribution $(x_1, y_1, z_0 - \epsilon)$ to a calculated $B_z(x_0, y_0, z_0)$. We start by showing the contribution of $(x_1, y_1, z_0 + \epsilon)$ to the infinitesimal change $dB_z(x_0, y_0, z_0)$,

$$dB(x_0, y_0, z_0)|_{(x_1, y_1, z_0+\epsilon)} =$$
$$-\frac{\mu_0}{4\pi}\sigma(x_1, y_1, z_0+\epsilon) \cdot \nabla u(x_1, y_1, z_0+\epsilon) \times \frac{(x_0, y_0, z_0)^T - (x_1, y_1, z_1+\epsilon)^T}{|(x_0, y_0, z_0)^T - (x_1, y_1, z_0+\epsilon)^T|^3} dV =$$
$$-\frac{\mu_0}{4\pi}\sigma(x_1, y_1, z_0) \cdot \nabla u(x_1, y_1, z_0) \times \frac{(x_0, y_0, z_0)^T - (x_1, y_1, z_0+\epsilon)^T}{|(x_0, y_0, z_0)^T - (x_1, y_1, z_0+\epsilon)^T|^3} dV =$$
$$-\frac{\mu_0}{4\pi}\sigma(x_1, y_1, z_0) \cdot \nabla u(x_1, y_1, z_0) \times \frac{(x_0 - x_1, y_0 - y_1, -\epsilon)^T}{|(x_0 - x_1, y_0 - y_1, -\epsilon)^T|^3} dV.$$

In the same manner, we arrive at the infinitesimal contribution from $(x_1, y_1, z_0 - \epsilon)$ to be

$$dB(x_0, y_0, z_0)|_{(x_1, y_1, z_0-\epsilon)} =$$
$$-\frac{\mu_0}{4\pi}\sigma(x_1, y_1, z_0) \cdot \nabla u(x_1, y_1, z_0) \times \frac{(x_0 - x_1, y_0 - y_1, \epsilon)^T}{|(x_0 - x_1, y_0 - y_1, \epsilon)^T|^3} dV.$$

Hence, we see that the vector on the left side of the cross product is equal for the two contributions. The vector on the right side of the cross product has the same denominator, as $|(x_0 - x_1, y_0 - y_1, \epsilon)| = |(x_0 - x_1, y_0 - y_1, -\epsilon)|$. Naming this denominator, d and the vector on the left hand side of the cross product, $\mathbf{a} = (a_1, a_2, a_3)$ and including the constant term into $\mathbf{a}$ we can calculate explicitly the contribution for each of the two mirrored points in space.

$$dB(x_0, y_0, z_0)|_{(x_1, y_1, z_0 + \epsilon)} = \mathbf{a} \times \frac{(\Delta x, \Delta y, \epsilon)^T}{d} dV = \begin{pmatrix} \frac{a_2 \epsilon - a_3 \Delta x}{d} \\ \frac{a_3 \Delta x - a_1 \epsilon}{d} \\ \frac{a_1 \Delta y - a_2 \Delta x}{d} \end{pmatrix} dV$$

$$dB(x_0, y_0, z_0)|_{(x_1, y_1, z_0 - \epsilon)} = \mathbf{a} \times \frac{(\Delta x, \Delta y, -\epsilon)^T}{d} dV = \begin{pmatrix} \frac{-a_2 \epsilon - a_3 \Delta x}{d} \\ \frac{a_3 \Delta x + a_1 \epsilon}{d} \\ \frac{a_1 \Delta y - a_2 \Delta x}{d} \end{pmatrix} dV$$

Adding the two contributions results in the following infinitesimal contribution to $B(\mathbf{r})$.

$$dB(x_0, y_0, z_0)|_{(x_1, y_1, z_0 \pm \epsilon)} = \begin{pmatrix} \frac{a_2 \epsilon - a_3 \Delta y}{d} \\ \frac{a_3 \Delta x - a_1 \epsilon}{d} \\ \frac{a_1 \Delta y - a_2 \Delta x}{d} \end{pmatrix} + \begin{pmatrix} \frac{-a_2 \epsilon - a_3 \Delta y}{d} \\ \frac{a_3 \Delta x + a_1 \epsilon}{d} \\ \frac{a_1 \Delta y - a_2 \Delta x}{d} \end{pmatrix} dV$$

$$= \begin{pmatrix} \frac{-2a_3 \Delta y}{d} \\ \frac{2a_3 \Delta x}{d} \\ \frac{2(a_1 \Delta y - a_2 \Delta x)}{d} \end{pmatrix} dV.$$

Here we apply the fact that $\mathbf{J}(x, y)$ and thus $\mathbf{a}$ has no z-component. Thereby the total contribution from two mirrored points to a single element is given by

$$dB(x_0, y_0, z_0)|_{(x_1, y_1, z_0 \pm \epsilon)} = \begin{pmatrix} 0 \\ 0 \\ \frac{2(a_1 \Delta y - a_2 \Delta x)}{d} \end{pmatrix} dV. \tag{3.67}$$

Thus, the z-component of the contribution is

$$dB_z(x_0, y_0, z_0) = \frac{2(a_1 \Delta y - a_2 \Delta x)}{d} dV, \tag{3.68}$$

with $\mathbf{a} = \frac{\mu_0}{4\pi}\mathbf{J}(\mathbf{r})$, $d = |\mathbf{r} - \mathbf{r}'|^3$ and $\Delta x = x_0 - x', \Delta y = y_0 - y'$.

Thus, if a symmetric infinitely object is simulated, one can find the contribution to the middle slice from only computing half the cylindrical object. Yet the computation of the total z-component of $\mathbf{B}$ is still cumbersome even when half the computations are sliced away. We can, however, use the above knowledge of the contributions to our advantage and set up a different way of computing B_z in a slice, z_0. First we look back at Maxwell's equation for the relation between the magnetic field strength, $\mathbf{H}$, and the current, $\mathbf{J}$ for time independent electromagnetic fields, (2.10) and (2.6) yields the following equality

$$\nabla \times \mathbf{H} = \mathbf{J} \Leftrightarrow$$
$$\nabla \times \mathbf{B} = \mu_0\mathbf{J}.$$

The above equation can be expanded using the definition of the curl operator.

$$\left(\frac{\partial B_z}{\partial y} - \frac{\partial B_y}{\partial z}\right) \cdot \mathbf{i} + \left(\frac{\partial B_x}{\partial z} - \frac{\partial B_z}{\partial x}\right) \cdot \mathbf{j} + \left(\frac{\partial B_y}{\partial x} - \frac{\partial B_x}{\partial y}\right) \cdot \mathbf{k} = \mu_0\mathbf{J}. \quad (3.69)$$

The above equation is just as horrible to solve as the volume integration of Biot-Savart's law, however, if we use the symmetric properties and the knowledge of the $\mathbf{B}$ only having a z-component from (3.68), we can apply Gauss' law of magnetic fields, (2.4) in its integral form given by

$$\oiint_S \mathbf{B} \cdot d\mathbf{A} = 0. \quad (3.70)$$

Where, $d\mathbf{A}$ is the unit outward normal to the surface, S. Gauss' law for magnetism states that magnetic flux entering a closed domain must also exit the closed domain. Now, by applying a square thin domain enclosing the infinite cylinder and noting that the magnetic flux inside the cylinder is only in the z-direction, the flux lines only enter and exit through the surface of the closed domain on the sides which has normal vectors in the $\pm$ z-direction. And these must then be equal. Moving one of these surfaces towards the other, i.e. letting the height of the closed domain go towards zero, we can conclude that the magnetic field must be constant in the z-direction.

We can now go back to (3.69) and set any component related to a change in the z-direction equal to 0 and applying that the B_x and B_y components are 0, while also splitting the current density into its components, yielding

$$\frac{\partial B_z}{\partial y} \cdot \mathbf{i} - \frac{\partial B_z}{\partial x} \cdot \mathbf{j} + 0 \cdot \mathbf{k} = \mu_0 J_x \cdot \mathbf{i} + \mu_0 J_y \cdot \mathbf{j} + \mu_0 0 \cdot \mathbf{k}. \qquad (3.71)$$

Rearranging reveals the partial differential equation

$$\nabla B_z(x, y) = \mu_0(-J_y, J_x). \qquad (3.72)$$

This partial differential equation has a unique solution if one point of B_z is known. This can be calculated by a single computation using Biot-Savart's law. This partial differential equation can be stated as

$$\nabla B_z(x, y) = \mu_0 \hat{J}, \ \text{ in } \Omega_0,$$
$$B_z = B_{BS}, \ \text{ in } \Omega_1,$$

where $\hat{J} = (-J_y, J_x)$, B_{BS} is B_z calculated from the Biot-Savart law and $\Omega_0 \cup \Omega_1 = \Omega|_{z=z_0}$. Assuming that B_z is smooth, we can multiply with a test function, $v \in H_0^1(\Omega)$ and integrate over the domain, Ω yielding

$$\int_{\Omega_0} \nabla B_z \cdot \nabla v \ dx = \int_{\Omega} \mu_0 \hat{J} \cdot \nabla v \ dx - \int_{\Omega_1} B_{BS} v \ dx, \ \ \forall v \in H_0^1(\Omega). \qquad (3.73)$$

□

The above derivations can be concatenated into a theorem:

THEOREM 3.5 *Iff* $\mathbf{x} \in \Omega \subset \mathbb{R}^3$*, with geometry of Ω defined by 3.4 and $J(\mathbf{x}) = -\sigma \nabla u(\mathbf{x})$ derived from the solution of 3.1 or 3.2, then (3.72) has a unique solution, $B_z(\mathbf{x}) \in H^1(\Omega)$ satisfying (3.73).*

3.3.2   Getting the 2D k-space data

After having computed the z-component of the magnetic flux density in a slice, z_0, it is now possible to calculate the incremental phase change, $\Psi(\mathbf{x})$, caused by $\mathbf{B}_z(\mathbf{x})$ in that same slice. This is done through equation (**??**) as

$$\Psi(\mathbf{x}) = 2\gamma B_z(\mathbf{x})T_{\mathbf{J}}. \tag{3.74}$$

This operation requires the choice of setting the time in which the current I_+ and I_- should be applied. The longer the time, $T_{\mathbf{J}}$ is applied the better the quality of B_z and also the bigger the phase-change will be, even at points where B_z might be small. I.e. a larger distortion and difference between different differences in conductivity will be seen. However, as mentioned earlier when the standard deviation of B_z was introduced, there are physiological aspects regarding the time that need be taken into account. Furthermore, we can compute the entire k-space data set, assuming a spin-echo sequence as explained earlier, i.e. a rectangular sampling of k-space. This is done simply by invoking the formula for the data by equation (2.33). As can be see from (2.33), the magnetization $\mathbf{M}(x, y, z_0)$ is involved. This magnetization is not necessarily connected to the conductivity, but rather the density of protons. One could choose, in simulations that no information was available from the transverse magnetization, however, in the interest of applying the theory of MREIT in an inverse algorithm, it is accepted that the transverse magnetization is known, and furthermore will be used as an edge definition for the mesh that the inverse problem solved on. This means that the transverse magnetization is capable of distinguishing different tissue types but not their conductivity.

$$S_{I_\pm}(\mathbf{k}) = \int_{\Omega_{z_0}} \mathbf{M}(x, y, z_0) e^{i(\pm\gamma B_z(x,y,z_0)T_{\mathbf{J}} + \delta(x,y,z_0))} e^{i(\mathbf{k}\cdot\mathbf{x})} d\mathbf{x}. \tag{3.75}$$

Noticeably, we have here avoided the computation of the two complex images, $m_{I_\pm}$. It is not necessary to compute the true k-space data. It can however, given known magnetization and choice of systematic phase error to introduce errors into each of these two complex images. This concludes the process of the forward problem. An effective forward problem formulation is essential to obtain a formulation of the inverse problem which is the aim of the next chapter.

CHAPTER 4

The Inverse Problem

This chapter will aim to formulate the inverse problem of acquiring the anisotropic conductivity distribution given measured B_z data. We will start by assuming that the domain, Ω in which a 2D slice of an anisotropic conductivity distribution is to be found consists of a section of an infinite cylinder with $\sigma(\mathbf{x})$ not changing along the z-axis and electrodes are placed continuously on the surface along the z-axis. This simplified domain allows the usage of the results found in 3.3.1.

4.1 Observability from B_z

Before diving into the setup of the inverse problem we must ask ourselves whether knowledge of B_z is enough. It turns out that it is not enough to have a single data-set of B_z available. This stems from looking at Biot-Savart's law, stated again below

$$B(\mathbf{r}) = \frac{\mu_0}{4\pi} \int_\Omega -\sigma(\mathbf{r}')\nabla u(\mathbf{r}') \times \frac{\mathbf{r}-\mathbf{r}'}{|\mathbf{r}-\mathbf{r}'|^3} \, d\mathbf{r}' \tag{4.1}$$

First off, it can be seen that if σ solves the above equation, so does a scaling

of that σ, i.e. $\alpha\sigma$. This is indeed only a problem if one chooses the complete electrode model as the forward model for the inverse problem and it is resolved by measuring a potential difference between any two boundary points. This is done a priori when using the pure Robin bc model. Secondly, any change of $\sigma(\mathbf{x})$ along the normal direction of the equipotential surfaces, ∇u, is invisible from B_z data. This can be seen by assuming a function $\phi : \mathbb{R} \to \mathbb{R}$ which is strictly increasing and continuously differentiable. Then $\phi(u)$ also solves the Boundary Value Problem posed by either CEM and Pure Robin BC when the conductivity is changed to $\sigma = \frac{\sigma}{\phi'(u)}$. This is because

$$\sigma(\mathbf{r}) \cdot \nabla u(\mathbf{r}) = \frac{\sigma(\mathbf{r})}{\phi'(u(\mathbf{r}))} \cdot \nabla \phi(u(\mathbf{r})). \tag{4.2}$$

This is true for any strictly increasing function. Thus, there are infinitely many conductivity distributions which satisfies the BVP and Biot-Savart's law for given B_z data. This was also the result seen from (3.72).

Lastly, we note that B_z data traces a change of σ along the tangent direction of the equipotential surfaces or the tangent direction of the vector field flow, $\sigma(\mathbf{x}) \cdot \nabla u(\mathbf{x})$. This follows directly from the partial differential equation found in (3.72) which can be rewritten in weak formulation by[WS11]

$$\int_\Omega B_z(\mathbf{x}) \cdot \eta(\mathbf{x}) d\mathbf{x} = \int_\Omega (\sigma(\mathbf{x})\nabla u(\mathbf{x})) \cdot \eta(\mathbf{x}) d\mathbf{x}, \quad \forall\, \eta \in \mathrm{C}_0^1. \tag{4.3}$$

It is known that the vector field $-\sigma\nabla u$, or the current density $\mathbf{J}$, is mainly based upon the positioning of the electrodes and the geometry of $\partial\Omega$. Thus, to overcome the directional change of $\sigma(\mathbf{x})$ which a single current density can observe, in MREIT, two or more linearly independent currents are passed through the object, so that the orthogonal directional change of $\sigma(\mathbf{x})$ can be observed. In general, N different currents originating from N pairs of electrodes can be passed through the object. However, time consumption during an MREIT experiment increases by $\frac{N}{2}$. Thus, usually two pairs of electrodes are utilized and placed such that the parallelogram spanned by the two vectors $\mathbf{J}_1 \times \mathbf{e}_z$ and $\mathbf{J}_2 \times \mathbf{e}_z$ is as large as possible. This corresponds to, if the object to be imaged is circular, a placement of electrodes with their centres exactly $\frac{\pi}{2}$ apart.

4.2   The Inverse Model

In this section the model governing the inverse problem of MREIT is presented. The model is based solely on data from the z-component of the magnetic field density attained from current densities generated by $N \geq 2$ pairs of electrodes on the object. The geometry of the model follows that of the previous sections, i.e. a section of an infinite cylinder with conductivity distribution independent of the z-variable and electrodes continuously on the surface in the z-direction. We assume that current is injected through a pair of electrodes, $\epsilon_j^{\pm}$, where $j = 1..N$. For a given elliptic anisotropic, symmetric conductivity distribution, $\sigma(\mathbf{x}) \in \mathbb{C}_+^{1,2\times2}(\bar{\Omega})$, the resulting potential distribution is denoted $u_j[\sigma]$, corresponding to $g_j(\mathbf{x})$ defined on the boundary from (3.10). Thus, $u_j[\sigma]$ solves the Pure Robin BC model

$$-\nabla \cdot (\sigma \nabla u_j[\sigma]) = 0, \quad \mathbf{x} \in \Omega,$$

$$u_j[\sigma] + z\sigma \frac{\partial u_j[\sigma]}{\partial \mathbf{n}} = g_j, \quad \mathbf{x} \text{ on } \partial\Omega.$$

We can then define a mapping, for $N = 2$, $\Lambda : C_+^{1,2\times2}(\bar{\Omega}) \to H^1(\Omega) \times H^1(\Omega) \times \mathbb{R} \times \mathbb{R}$ such that,

$$\Lambda[\sigma](\mathbf{x}) = \begin{pmatrix} \mu_0 \left(-\sigma \nabla u_1[\sigma]\right) \times \mathbf{e}_z \\ \mu_0 \left(-\sigma \cdot \nabla u_2[\sigma]\right) \times \mathbf{e}_z \\ \frac{\mu_0}{4\pi} \int_\Omega \frac{\langle \mathbf{x_0} - \mathbf{x}', -\sigma(\mathbf{x}') \cdot \nabla u_1[\sigma](\mathbf{x}') \times \mathbf{e}_z \rangle}{|\mathbf{x_0} - \mathbf{x}'|^3} d\mathbf{x}' \\ \frac{\mu_0}{4\pi} \int_\Omega \frac{\langle \mathbf{x_0} - \mathbf{x}', -\sigma(\mathbf{x}') \cdot \nabla u_2[\sigma](\mathbf{x}') \times \mathbf{e}_z \rangle}{|\mathbf{x_0} - \mathbf{x}'|^3} d\mathbf{x}' \end{pmatrix} . \tag{4.4}$$

This mapping then consists of $\Lambda_1 = \nabla B_{1,z}$, $\Lambda_2 = \nabla B_{2,z}$, $\Lambda_3 = B_{1,z}(\mathbf{x_0})$, $\Lambda_4 = B_{2,z}(\mathbf{x_0})$. $\Lambda_{3,4}$ are then the gauges to the solution which identifies a unique solution of B_z. On the basis of Λ and (3.73) we can now pose a new mapping, $\Gamma : H^1(\Omega) \times H^1(\Omega) \times \mathbb{R} \times \mathbb{R} \to H^1(\Omega) \times H^1(\Omega)$ as

$$\Gamma[\Lambda[\sigma]] = \begin{pmatrix} \text{solve}(\Lambda_1[\sigma], \Lambda_3[\sigma]) \\ \text{solve}(\Lambda_2[\sigma], \Lambda_4[\sigma]) \end{pmatrix} = \begin{pmatrix} B_{1,z}(x, y, z_0) \\ B_{2,z}(x, y, z_0) \end{pmatrix} . \tag{4.5}$$

Now, $\Gamma[\Lambda[\sigma]] = (B_{1,z}, B_{2,z})^T$. The aim of the inverse problem of MREIT is now

to find a σ from data of $B_{j,z}$ which minimizes

$$\Phi(\sigma) = \sum_{j=1}^{N} \|\Gamma_j[\Lambda[\sigma]] - B_{j,z}\|^2_{L^2(\Omega)}. \tag{4.6}$$

Where $B_{j,z}$ is now the data attained from the current densities, $\mathbf{J}_j$.

4.3 Uniqueness of the Inverse Model

It is vital that the model for the inverse problem is unique, s.t. the only difference between finding the optimal conductivity distribution lies in computational errors and the optimization process. Uniqueness of the model can be showed that if $\Gamma[\Lambda[\sigma]] = \Gamma[\Lambda[\tilde{\sigma}]] \Leftrightarrow \sigma = \tilde{\sigma}$. Uniqueness for 3 dimensions is yet to be established but through an analogue to the proof of uniqueness using full Biot-Savart in the mapping, Λ [WS11], uniqueness can be established in 2D under the geometric setup given by 3.4. First we denote $u_j[\sigma] = u_j$ and $u_j[\tilde{\sigma}] = \tilde{u}_j$. Now, by taking the laplacian of $\Gamma_j[\Lambda[\sigma]] = \Gamma_j[\Lambda[\tilde{\sigma}]]$, $j = 1, 2$ yields

$$\Delta\Gamma_j[\Lambda[\sigma]] = \Delta\Gamma_j[\Lambda[\tilde{\sigma}]] \Leftrightarrow$$
$$\nabla \cdot (\mu_0 (-\sigma\nabla u_j) \times \mathbf{e}_z) = \nabla \cdot (\mu_0 (-\tilde{\sigma} \cdot \nabla\tilde{u}_j) \times \mathbf{e}_z) \Leftrightarrow$$
$$0 = \nabla \cdot [(\sigma\nabla u_j) \times \mathbf{e}_z - (\tilde{\sigma} \cdot \nabla\tilde{u}_j) \times \mathbf{e}_z] \Leftrightarrow$$
$$0 = \nabla_{xy} \times \left[\sigma \cdot \frac{\partial u_j}{\partial x} - \tilde{\sigma} \cdot \frac{\partial \tilde{u}_j}{\partial x}, \sigma\frac{\partial u_j}{\partial y} - \tilde{\sigma} \cdot \frac{\partial \tilde{u}_j}{\partial y}\right].$$

Herein comes the 2D proof only, as $\nabla_{xy} = [\frac{\partial}{\partial x}, \frac{\partial}{\partial y}]$, the two-dimensional gradient. Hence, a scalar function, $\phi_j(\mathbf{x})$ exists such that

$$\nabla_{xy}\phi_j(\mathbf{x}) = \left[\sigma \cdot \frac{\partial u_j}{\partial x} - \tilde{\sigma} \cdot \frac{\partial \tilde{u}_j}{\partial x}, \sigma\frac{\partial u_j}{\partial y} - \tilde{\sigma} \cdot \frac{\partial \tilde{u}_j}{\partial y}\right], \quad \mathbf{x} \in \Omega.$$

Then ϕ_j satisfies the laplace equation, $\Delta_{x,y}\phi_j = 0$, $\mathbf{x} \in \Omega$ with zero Neumann condition. Hence, ϕ_j must be constant. [WS11] states that (4.3) is equivalent

to

$$\Delta B_z = \nabla \ln(\sigma) \cdot (\sigma \nabla u \times \mathbf{e}_z) . \tag{4.7}$$

Using this and $\sigma \nabla u_j = \tilde{\sigma} \cdot \nabla \tilde{u}_j = \Delta_{xy} \phi_j = 0$, we can derive the system

$$\begin{bmatrix} \sigma \frac{\partial u_1}{\partial x} & -\sigma \frac{\partial u_1}{\partial y} \\ \sigma \frac{\partial u_2}{\partial x} & -\sigma \frac{\partial u_2}{\partial y} \end{bmatrix} \begin{bmatrix} \frac{\partial}{\partial y} \ln \frac{\sigma}{\tilde{\sigma}} \\ \frac{\partial}{\partial x} \ln \frac{\sigma}{\tilde{\sigma}} \end{bmatrix} = \begin{bmatrix} 0 \\ 0 \end{bmatrix} . \tag{4.8}$$

[WS11] states that the left matrix is invertible for all $\mathbf{x} \in \Omega$. Thus, $\sigma = c\tilde{\sigma}$. We then take a look at the boundary condition which both u_j and $\tilde{u}_j$ upholds and state it for both of them.

$$u_j + z\sigma \frac{\partial u_j}{\partial \mathbf{n}} = g_j$$

$$\tilde{u}_j + zc\tilde{\sigma} \cdot \frac{\partial \tilde{u}_j}{\partial \mathbf{n}} = g_j.$$

which gives by subtracting the two equations from each other

$$u_j - \tilde{u}_j + z\sigma \frac{\partial u_j}{\partial \mathbf{n}} - zc\tilde{\sigma} \cdot \frac{\partial \tilde{u}_j}{\partial \mathbf{n}} = 0.$$

Hence, if u_j and $\tilde{u}_j$ solves the BVP of (3.9)-(3.10) which has a unique solution, then $u_j - \tilde{u}_j = 0$ and $\frac{\partial u_j}{\partial \mathbf{n}} - \frac{\partial \tilde{u}_j}{\partial \mathbf{n}} = 0$, hence, $c = 1$ and uniqueness is established.

4.4   The Optimization

This section will explain the process of the optimization including choice of algorithm and modelling parameters. First of all the experiments are constrained to the scenario of known borders of the sub-domains inside, Ω. Thus, it is assumed that the transverse magnetization MR image, $M_0 e^\phi$ is of good enough quality to distinguish the borders between different tissue types, specifically it is assumed that the transverse magnetization is of the quality presented in [MWT11]. Hence we restrict ourselves to solving a problem of finding $\{\sigma_k\}_{k=1}^{K}$

where K is the number of different sub-domains inside Ω. Secondly, the experiments will be restricted to experiments from 2 and 3 sets of electrodes placed equidistantly on the boundary $\partial\Omega$. Three different sizes of noise is used in the experiments, 0%, 1% and 10%. The noise is considered Gaussian white noise with the same distribution throughout Ω. This specific assumption is discussed later in the thesis. The additive error is thus calculated as follows:

$$\mathrm{err}_j[n] = \alpha \frac{e[n]}{\|e\|_2} \|B_{j,z}\|_2.$$

Here α is the degree of the noise, i.e. for $1\% \Leftrightarrow \alpha = 0.01$, $e[n] \sim N(0,1)$. e is a vector containing all e_n, one for each node in the discretization of the domain, Ω and $B_{j,z}$ is the B_z data for the j'th pair of electrodes.

4.4.1 Optimization Algorithm and parameters

The choice of optimization algorithm falls down to a choice between very few algorithms. We require an algorithm which can handle non-linear optimization. Furthermore, we require an algorithm which can take bounds for parameter values as input. Lastly, the algorithm should not need a user-supplied gradient, since this, in the problem at hand, is impossible to provide. Thus, we need a gradient-free algorithm for constrained non-linear optimization. Furthermore, the numerical solutions of the PDEs presented in the thesis is solved using the FEniCS [LMea12][LW10][KL06][ALO+13][ALM+09][Kir04] packages for the programming language, Python. Thus, we need an algorithm which is implemented in Python. Using those criteria we arrive at the following three algorithms to choose from for constrained non-linear optimization:

- L-BFGS-B
- COBLYA
- SLSQP

The COBLYA algorithm uses linear approximation to the objective function and initial testing when using this algorithm was unfruitful and it was discarded from further use. The SLSQP algorithm uses sequential least squares programming. Because of a lack of knowledge on this algorithm it was discarded from further use. The parameters available for the optimization call was also not lucrative compared to the last option. Lastly, the L-BFGS-B algorithm [BLN95] was

taken into use. This choice was also my first choice since I had experience implementing a regular BFGS algorithm during my studies. The algorithm is a part of the Scientific Python optimize package and has a vast number of parameters that can be utilized in the optimization strategy. The parameters used are the following:

- APPROXGRAD - "True"/"False" decides whether the algorithm should numerically approximate the gradient. This is set to "True"

- BOUNDS - a list of (x_{min}, x_{max}) for the optimization parameters, x. If either the upper bound or the lower bound is not known, it can be set to "None". In the testing all diagonal elements of σ_j are set to $x_{min} = 0.05$ and all non-diagonal elements are set to 0. The upper bounds are chosen to be somewhat larger than the maximum value of σ.

- FACTR - scalar value which acts as a stopping criteria for the iteration when $\frac{f^k - f^{k+1}}{\max\{|f^k|, |f^{k+1}|, 1\}} \leq \text{factr} * \text{eps}$, where eps is the machine precision.

- PGTOL - The projected gradient tolerance. The iteration stops when $\max\{|\text{pg}_i|, \ i = 1, ..., n\} \leq \text{pgtol}$, where pg_i is the i-th component of the projected gradient.

- M - integer defining how much of the Hessian matrix is stored in the memory. Thus, it defines the precision of the algorithm, 10 is large precision, 1 is less precision, etc.

- EPSILON - The step size for finite difference approximation to the gradient.

- MAXFUN - integer defining the maximum number of function evaluations before termination.

Due to the fact that the problem of finding the correct conductivity distributions is highly non-linear, the objective function will contain many local minima. Therefore a sequence of optimization routines are run for each experiment with increasing precision and decreasing FACTR/PGTOL together with a decreasing stepsize. The inital stepsize is chosen large enough s.t. a step for each parameter, x will contain the true value. After that sequential lowering of the stepsize is done to attain convergence to towards the true σ distribution.

Finally, the algorithm will work towards minimizing the total objective function (4.6), however, vital information lies in examining the individual objective

functions for each set of electrodes given by

$$\Phi_j = \|\Gamma_j[\Lambda[\sigma]] - B_{j,z}\|^2_{L^2(\Omega)}. \tag{4.9}$$

A good solution will show an almost equal value for $j = 1..N$ and this value should be of the order of $\|e\|^2_2$, i.e. the sum of all noise squared. This value is available during computer simulations but not available in practical experiments. However, the fact that all individual loss functions, (4.9), should be of the same order of magnitude is available. More on this subject will be discussed as a consequence of one the later experiments.

4.5   Benchmark test

This section aims to test the optimization strategy in the setting of an isotropic conductivity distribution. This is because there are no functional algorithms for MREIT with assumed anisotropic conductivity distribution. The closest attempt at such an algorithm is in [PPKW04]. In simulations of very simple domains the algorithm successfully reconstructed the conductivity tensor distribution, however, because the algorithm is very sensitive to noise, it fails with the SNR(Signal to Noise Ratio) becomes less than ideal which is the case of practical MREIT. Thus, it is of interest to test the current minimization strategy against the current applicable MREIT software on the market. The leading software package for in-vivo MREIT is that of CoReHA 2.0. CoReHA 2.0 applies a local harmonic B_z algorithm and several preprocessing algorithms and has shown to be able to reconstruct an accurate scaled isotropic conductivity image. Hence, the first experiment will be to shown that a general optimization scheme can indeed also produce accurate isotropic conductivity images from simulated data. The experiment is conducted with 0%,1% and 10% noise levels. The domain that the solution is sought for is distinguished into a background conductivity and two disc objects with different conductivities and sizes. In figure 4.1, the sub-domains with different conductivities is shown. The actual values do not correspond to those of the experiments. conductivity distribution is shown. Three sets of electrodes are equidistantly distributed on $\partial\Omega$. Throughout the experiments the estimated parameters and true parameters will be referred to by their respective domain and placement in the conductivity tensor. Thus, isotropic conductivity parameters will be referred to as $\Omega_1, .., \Omega_3$ for three different sub-domains and anisotropic parameters will have an extra subscript denoting their position in the tensor. Thus, Ω_{11} refers to sub-domain number 1 and $\sigma_{1,1}$ in the associated tensor, Ω_{12} will refer to $\sigma_{1,2}$ and $\sigma_{2,1}$ for sub-domain number 1.
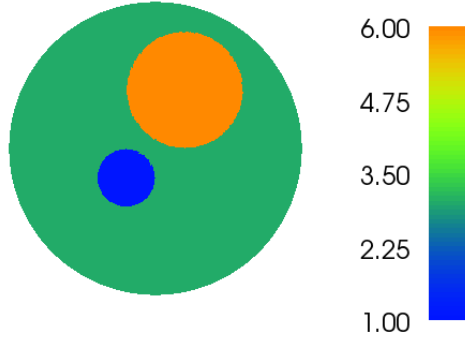
Figure 4.1: Boundary layout for conductivity distribution, σ
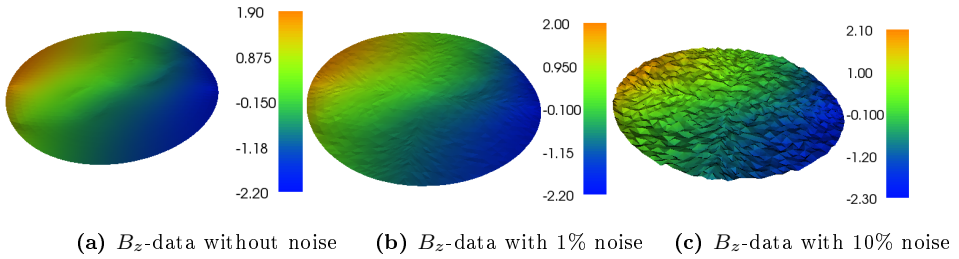
(a) B_z-data without noise   (b) B_z-data with 1% noise   (c) B_z-data with 10% noise

Figure 4.2: Sample of data sets for experiments

In figure 4.2 a sample of the data for each experiment is shown. From these it is possible to see the outlines of the interior sub-domains in the data-set without noise. However, it becomes increasingly difficult with increasing noise level.

4.5.1   Benchmark 0% noise

Below in table 4.1 are the results of the benchmark test when data is not corrupted by noise. The step-size for finite difference approximation of the gradient/Hessian is denoted ϵ and will be done so for all tables throughout the result-section.

As can be seen, the initial guess, σ_0 is relatively close to the true $\sigma^\star$. It is

0%	ϵ	Ω_1	Ω_2	Ω_3
σ_0		1.2	5.8	0.7
σ_1	1.00	0.98495	5.20950	0.612739
σ_2	0.50	0.98495	5.20950	0.612739
σ_3	0.25	0.98495	5.20950	0.612739
σ_4	0.10	0.98495	5.20950	0.612739
σ_5	0.01	0.99481	6.30462	0.487782
$\sigma^\star$		1.0	6.0	0.5

Table 4.1: Convergence pattern for σ with incrementally smaller stepsizes $[1, 0.5, 0.25, 0.1, 0.01]$. $\sigma^\star$ is true conductivity. Each column represent individual convergence for each sub-domain. 0% noise added

noticeable that no changes happen to the conductivity distribution for stepsizes, $0.5 \rightarrow 0.1$. The algorithm fails to find any search direction which is beneficial to minimizing the object function. However, we see that for stepsize 0.01, a large jump in solution occurs which makes σ_5 for Ω_1 and Ω_3 become very close to the true conductivities. However, the difference seems larger for Ω_2. This phenomenon will be explored in section **??**. However, the relative difference between the true $\sigma^\star|_{\Omega_2}$ is only 5%. In the two following sections, noise will be added to the data to see if the algorithm can find a good solution with noisy data.

4.5.2   Benchmark 1% noise

In this simulation, the same parameters are used, except the noise level, α is now increased to 1% from 0%. This yields the table of convergence seen in 4.2

Comparing table 4.1 and 4.2, the final result is not much different. there is still a relative difference of almost 5% for $\sigma \in \Omega_2$, however, the relative difference between the solution and the true conductivity of Ω_3 is now increased to almost 11%. The conductivity distribution of the largest sub-domain $\sigma \in \Omega_1$ is still very well approximated. One aspect to take notice of is that the solution parameters now change for each step-size and does not simply take one big leap for the smallest step-size.

1%	ϵ	Ω_1	Ω_2	Ω_3
σ_0		0.8	6.2	0.3
σ_1	1.00	0.8	6.2	0.3
σ_2	0.50	0.83180	6.23459	0.44795
σ_3	0.25	0.89410	6.24993	0.51360
σ_4	0.10	0.97665	6.27026	0.55604
σ_5	0.01	0.99148	6.27081	0.55497
$\sigma^\star$		1.0	6.0	0.5

Table 4.2: Convergence pattern for σ with incrementally smaller step-sizes $[1, 0.5, 0.25, 0.1, 0.01]$. $\sigma^\star$ is true conductivity. Each column represent individual convergence for each sub-domain. 1% noise added

4.5.3 Benchmark 10% noise

In this simulation the optimization parameters are kept form the previous two simulations and the noise level is now $\alpha = 0.1 = 10\%$. The convergence table is seen in 4.3

10%	ϵ	Ω_1	Ω_2	Ω_3
σ_0		0.8	6.2	0.3
σ_1	1.00	0.8	6.2	0.3
σ_2	0.50	0.82543	6.20636	0.32719
σ_3	0.25	0.97734	6.24433	0.48965
σ_4	0.10	0.97734	6.24433	0.48965
σ_5	0.01	1.00027	6.24585	0.49396
$\sigma^\star$		1.0	6.0	0.5

Table 4.3: Convergence pattern for σ with incrementally smaller stepsizes $[1, 0.5, 0.25, 0.1, 0.01]$. $\sigma^\star$ is true conductivity. Each column represent individual convergence for each sub-domain. 10% noise added

From table 4.3 we see the un-suspected behaviour that the final estimate of the solution parameters is better than that of both 0% and 1% noise. However, the solution is comparable to that of 0% noise in 4.1 with only a slightly better result for all sub-domains. From these three simulations, we can conclude the following:

- In a simple domain structure the optimization using 3 data sets, $B_{1,z}, B_{2,z}, B_{3,z}$ from three pairs of electrodes equidistantly placed on $\partial\Omega$, the algorithm

performs admirably.

- It seems that a high contrast between the individual sub-domains results in a small bias in the estimated solution parameters.

- Noise in the data seems to have a stabilizing effect on the sequential convergence of different step-sizes, revealing a very good estimate for 10% noise.

4.6   Contrast sensitivity

We saw in section 4.5 that there seemed to be trouble with estimating the conductivity distribution when there was a large difference in conductivity between the sub-domains. In this section we show the results when the difference is smaller. The conductivity is in this section kept isotropic in all sub-domains. Only results for 1% and 10% noise are shown. First off we take a look at the results for 1% noise level:

1%	ϵ	Ω_1	Ω_2	Ω_3
σ_0		0.8	2.5	0.3
σ_1	1.00	0.8	2.5	0.3
σ_2	0.50	0.86397	2.53807	0.37158
σ_3	0.25	0.95315	2.59116	0.47139
σ_4	0.10	0.98013	2.60722	0.49169
σ_5	0.01	0.99251	3.05212	0.50027
$\sigma^\star$		1.0	3.0	0.5

Table 4.4: Convergence pattern for σ with incrementally smaller stepsizes $[1, 0.5, 0.25, 0.1, 0.01]$. $\sigma^\star$ is true conductivity. Each column represent individual convergence for each sub-domain. 1% noise added

It can be seen from table 4.4 that the sequential estimated parameters for smaller step-sizes converge in a nice manner towards the true parameters. The problem domain of Ω_2 from 4.5 in this sequence seems to be modelled quite well and the relative error is down to under 2% after the final optimization step and this is the largest of the relative errors between estimated and true conductivities. Next we take a look when the noise level is at 10% in table 4.5:

10%	ϵ	Ω_1	Ω_2	Ω_3
σ_0		0.8	2.5	0.3
σ_1	1.00	0.8	2.5	0.3
σ_2	0.50	0.86219	2.53702	0.36960
σ_3	0.25	0.95333	2.59127	0.47159
σ_4	0.10	0.97885	2.60646	0.48847
σ_5	0.01	0.99426	3.01717	0.48752
$\sigma^\star$		1.0	3.0	0.5

Table 4.5: Convergence pattern for σ with incrementally smaller stepsizes $[1, 0.5, 0.25, 0.1, 0.01]$. $\sigma^\star$ is true conductivity. Each column represent individual convergence for each sub-domain. 10% noise added

4.5 reveals the same behaviour as table 4.4, however the estimated parameter for Ω_2 is now as close to the true value as can be expected. However, this comes at the loss of some accuracy for $\sigma \in \Omega_3$. Both estimated conductivities are, however, still very good. From this section we have learned the following:

- The contrast between conductivities within sub-domains play a vital role in the accuracy of the estimated parameters. Lower contrast means better estimation.

- The noise level seems to have little effect on the final estimated parameters.

4.7 Anisotropic Conductivity Distribution

As the goal of the thesis is to investigate the properties of MREIT for anisotropic conductivity distributions, this section will show the results of fitting anisotropic conductivity distributions to data originating from anisotropic sub-domains. The true background, Ω_1, conductivity is simulated as being isotropic whereas the two sub-domains, Ω_2 and Ω_3 are both anisotropic. This yields a total of 9 parameters to be estimated without initial knowledge of whether a sub-domain is isotropic or anisotropic. The experiments done in this section are divided into three. First off, we explore the case of modelling data from anisotropic conductivity with a model consisting of isotropic conductivities. Secondly, we explore the impact of internal sub-domain geometry on the solution and lastly we explore the affect of less data for the optimization routine, i.e. one less pair of electrodes.

4.7.1   Isotropic Initial Guess

This section aims to show that treating the sub-domains as having isotropic conductivity when they truly are anisotropic is a bad idea. The simulation is done by generating data and adding noise using the true anisotropic conductivity parameters. Then a solution is sought by assuming that all domains are isotropic. Next using the result of the estimated isotropic parameters are utilized as starting guess for an anisotropic optimization. Thus, the starting guess for the anisotropic optimization sequence is made from $\sigma_{\text{IsoEstimate}} = [\sigma_1^{\text{iso}}, \sigma_2^{\text{iso}}, \sigma_3^{\text{iso}}]$ as follow:

$$\sigma_0^{\text{anisotropic}} = \left\{ \begin{bmatrix} \sigma_1^{\text{iso}} & 0 \\ 0 & \sigma_1^{\text{iso}} \end{bmatrix}, \begin{bmatrix} \sigma_2^{\text{iso}} & 0 \\ 0 & \sigma_2^{\text{iso}} \end{bmatrix}, \begin{bmatrix} \sigma_3^{\text{iso}} & 0 \\ 0 & \sigma_3^{\text{iso}} \end{bmatrix} \right\}. \tag{4.10}$$

In the tables 4.6 and 4.8 are the resultant estimates for both optimization routines. Both tests are made with a noise level of $\alpha = 0.1 = 10\%$.

10%	ϵ	Ω_1	Ω_2	Ω_3
σ_0		1.3	3.0	3.5
σ_1	1.00	0.1827	0.4486	0.4981
σ_2	0.50	0.2317	0.4949	0.4936
σ_3	0.25	0.3392	0.4849	0.4836
σ_4	0.10	0.3953	0.05	0.05
σ_5	0.01	0.4549	0.05	5.

Table 4.6: Convergence pattern for isotropic σ with incrementally smaller step-sizes $\epsilon = [1, 0.5, 0.25, 0.1, 0.01]$. True conductivity is anisotropic. Each column represent individual convergence for each sub-domain. 10% noise added. σ estimated as isotropic when real is anisotropic

From table 4.6 it can be seen that the optimization fails horribly in the last two runs which are supposed to be the most accurate. It is possible to see why the optimization fails if a look on the object function for each of the pairs of electrodes is taken. In table 4.7 we see that even though the optimization finds a better loss function for the three first runs, the three values related to each data-set are not comparable and thus, the estimated parameter fails to describe all three electrode configurations. This stems from the fact that isotropic conductivity can never satisfy all directions of current when the true current is based on anisotropic conductivity. However, the resultant estimated isotropic conductivities are applied to the initial guess for the anisotropic optimization routine yielding the results in 4.8

σ from 4.6	Φ_1	Φ_2	Φ_3	$\sum_{j=1}^{3} \phi_j$
σ_1	703	1887	588	3178
σ_2	562	1496	468	2527
σ_3	374	962	315	1642
σ_4	548	1293	503	2345
σ_5	404	918	390	1713

Table 4.7: Object functions for each pair of electrodes and hence each data set.

10%	ϵ	Ω_{11}	Ω_{12}	Ω_{13}	Ω_{21}	Ω_{22}	Ω_{23}
σ_0		0.4549	0.00	0.4549	0.05	0.0	0.05
σ_1	1.00	0.05	0.0	0.05	6.1696	0.0	1.9416
σ_2	0.50	0.9866	0.0	0.9868	6.3068	0.00000008	2.5114
σ_3	0.25	0.9866	0.0	0.9868	6.3068	0.00000008	2.5114
σ_4	0.10	0.9866	0.0	0.9868	6.3068	0.00000008	2.5114
σ_5	0.01	0.9661	0.0	1.0080	6.2365	0.0	2.9889
$\sigma^\star$		1.0	0.0	1.0	5.0	0.0	3.0
		Ω_{31}	Ω_{32}	Ω_{33}			
σ_0		5.0	0.0	5.0			
σ_1	1.00	5.2140	0.6300	4.0819			
σ_2	0.50	5.2213	0.6392	4.1453			
σ_3	0.25	5.2213	0.6392	4.1453			
σ_4	0.10	5.2213	0.6392	4.1453			
σ_5	0.01	5.1138	0.6058	4.1553			
$\sigma^\star$		2.5	0.0	4.0			

Table 4.8: Convergence pattern for σ with incrementally smaller step-sizes, $\epsilon = [1, 0.5, 0.25, 0.1, 0.01]$. $\sigma^\star$ is true conductivity. Each column represent individual convergence for each sub-domain. 10% noise added. Data from three sets of electrodes. Isotropic starting guess, σ_0

From table 4.8 some surprising results occur. Even though the starting guesses were completely wrong and very far from the true conductivities, the resulting estimates are changed several orders of magnitude and successfully manages to estimate the conductivity tensor for Ω_1. Again we see a problem with the high contrast between sub-domains which results in a bad estimate for Ω_{21} but surprisingly the other two parameters of Ω_{22} and Ω_{23} are both very well estimated compared to their initial guess. Almost all parameters of the conductivity ten-

sor for Ω_3 are poorly estimated. From this experiment, three vital lessons are learned:

- Estimating an isotropic conductivity distribution from data originating from materials exhibiting anisotropic conductivities results in bad estimates compared to estimating anisotropic conductivities.

- The algorithm has a high likelihood of reaching the bounds on the parameters when estimating isotropic conductivity from anisotropic data.

- The individual object functions give information which points to anisotropic conductivity in one or more domains.

4.7.2 Number of Electrodes

This section will explore the effect of the amount of data used to estimate the parameters. Specifically, the effect of decreasing the number of electrodes to two pairs from three pairs, as the previous experiments have been conducted with. Obviously, it will be expected that the estimated parameters will be further from the true conductivities. First, the results for applying three pairs of electrodes are shown. The larger step-sizes of 1.00 and 0.50 are removed as they gave no changes and failed during the optimization routine.

10%	ϵ	Ω_{11}	Ω_{12}	Ω_{13}	Ω_{21}	Ω_{22}	Ω_{23}
σ_0		0.8	0.0	1.2	4.0	0.5	3.6
σ_1	0.25	0.9104	0.0	1.0784	4.052	0.4863	3.5979
σ_2	0.10	0.9652	0.0	1.0102	4.0822	0.4562	3.5957
σ_3	0.01	0.9964	0.0	1.0045	4.9922	0.0	2.9283
$\sigma^\star$		1.0	0.0	1.0	5.0	0.0	3.0
		Ω_{31}	Ω_{32}	Ω_{33}			
σ_0		3.0	0.0	5.0			
σ_1	0.25	3.0043	0.0010	4.9937			
σ_2	0.10	2.9985	0.0022	4.9911			
σ_3	0.01	2.4191	0.0	4.8070			
$\sigma^\star$		2.5	0.0	4.0			

Table 4.9: Convergence pattern for σ with incrementally smaller step-sizes, $\epsilon = [1, 0.25, 0.1, 0.01]$. $\sigma^\star$ is true conductivity. Each column represent individual convergence for each sub-domain. 10% noise added. Data from three sets of electrodes

In table 4.9 it can be seen that the estimated anisotropic conductivities fit quite well with the true conductivities. However, $\sigma_{2,2}$ for Ω_3 is relatively far from the true value, namely 20%. It is also noticeable that this specific parameter had an initial guess that was quite a lot further from the true value than any of the other initial guesses. Let us now take a look at the estimation when there are only two pairs of electrodes with associated B_z-data available. The exact same initial guesses are made from the beginning.

10%	ϵ	Ω_{11}	Ω_{12}	Ω_{13}	Ω_{21}	Ω_{22}	Ω_{23}
σ_0		0.8	0.0	1.2	4.0	0.5	3.6
σ_1	0.25	0.8865	0.0	0.9148	4.0029	0.6071	3.5268
σ_2	0.10	0.9180	0.0	0.9463	4.0109	0.6044	3.5336
σ_3	0.01	0.9762	0.0144	0.9661	5.1080	0.0	3.6818
$\sigma^\star$		1.0	0.0	1.0	5.0	0.0	3.0
		Ω_{31}	Ω_{32}	Ω_{33}			
σ_0		3.0	0.0	5.0			
σ_1	0.25	3.0270	0.0106	4.9951			
σ_2	0.10	3.0266	0.0132	4.9957			
σ_3	0.01	2.5062	0.5134	4.9529			
$\sigma^\star$		2.5	0.0	4.0			

Table 4.10: Convergence pattern for σ with incrementally smaller step-sizes, $\epsilon = [0.25, 0.1, 0.01]$. $\sigma^\star$ is true conductivity. Each column represent individual convergence for each sub-domain. 10% noise added. Data from two sets of electrodes

It can be seen from table 4.10 compared to table 4.9 that for the first two sub-domains (6 parameters), accuracy is greatly reduced in table 4.10. Furthermore, in the last sub-domain, Ω_3, it can be seen that the parameter $\sigma_{11} \in \Omega_3$ is better estimated than was the case for table 4.9, however, the algorithm was not able to realize that the sub-domain, Ω_3 had a 0 in its off-diagonal element, as it could when having three pairs of electrodes. From this section we have learned the following:

- There is a great need for good initial guesses for every parameter if a good estimation is to be expected.

- Having only two pairs of electrodes significantly reduces the optimization routine's ability to estimate parameters well and specifically looses capability of determining off-diagonal elements of the conductivity in smaller domains, as Ω_3.

4.7.3 Sub-domain Geometry Sensitivity

In this section the effect of a different sub-domain geometry is explored. To do so, a simulation is run with two pairs of electrodes with the same settings as in the simulation in table 4.9. The sub-domain, Ω_3 is now a rectangle of the same area as the previous circular Ω_3. The new conductivity layout can be seen in figure 4.3. The idea of the experiment is that of testing the observability of B_z 4.1. A rectangle will have more current flowing tangentially to the sub-domain border than a disc object, and thus it will be expected that a poorer estimate will be made from a rectangular sub-domain with the same conductivity distribution. In table 4.11 the results for two sets of electrodes are shown. In 4.3 the new geometry of the imaging object is shown.
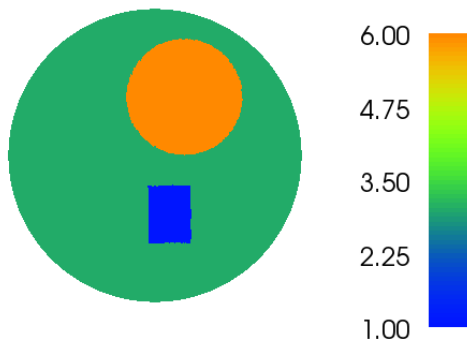
Figure 4.3: Boundary layout for conductivity distribution, σ

By comparing table 4.11 with the results for two electrode pairs with a disc-shaped Ω_3 the results are clearly worse for the rectangular shaped Ω_3. This is mostly visible for the estimated parameters of Ω_3, but these bad estimates are carried over and affect the estimates of the other sub-domains. However, this might be cause by the sub-domain positioning which is not entirely the same ?? and ??. Thus, from this experiment we learn that interior geometry affects estimation of anisotropic conductivity.

10%	ϵ	Ω_{11}	Ω_{12}	Ω_{13}	Ω_{21}	Ω_{22}	Ω_{23}
σ_0		0.8	0.0	1.2	4.0	0.5	3.6
σ_1	0.25	0.9268	0.0	0.9620	3.9942	0.6632	3.5084
σ_2	0.10	0.9377	0.0	0.94623	4.0132	0.6517	3.5089
σ_3	0.01	0.9811	0.0131	0.9504	4.5851	0.0524	3.5657
$\sigma^\star$		1.0	0.0	1.0	5.0	0.0	3.0
		Ω_{31}	Ω_{32}	Ω_{33}			
σ_0		3.0	0.0	5.0			
σ_1	0.25	3.0102	0.0424	4.9507			
σ_2	0.10	3.0077	0.0473	4.9490			
σ_3	0.01	2.8351	0.2028	4.8884			
$\sigma^\star$		2.5	0.0	4.0			

Table 4.11: Convergence pattern for σ with incrementally smaller step-sizes, $\epsilon = [0.25, 0.1, 0.01]$. $\sigma^\star$ is true conductivity. Each column represent individual convergence for each sub-domain. 10% noise added. Data from two sets of electrodes

4.8   Discussion

In the previous sections we have explored several aspects of both the general method of using optimization as a method of solving the inverse problem of MREIT and the complications of having to estimate an anisotropic conductivity distribution. In the above results section, there has been no mention of time consumption. All of the above experiments have been extremely time consuming when run on a Dell Latitude 5400 laptop. Some of the experiments used 20 hours of computational time before the optimization routine converged. This is perhaps the biggest draw-back of using an optimization scheme to estimate parameters. We have learned in several of the experiments that the initial guesses have a large influence on the final parameter estimation. It is thus essential that several starting guesses are applied to be certain that the algorithm has not found a bad local minimum and got stuck there. Thus, optimization sequences should be run. In each sequence, when doing non-linear constrained optimization, the gradient and to some extent, the Hessian needs to be numerically evaluated. This is a big process when the forward model is as complicated as it is using (4.5). In the process of applying (4.5) several linear variational systems are solved which all contribute with truncation errors. For each set of electrodes, 6 variational problems are solved. One to attain the potential distribution, one to gain the current distribution from said potential distribution and one to compute the resulting B_z field. The most time consuming part is, however, the small part of the domain which needs to have B_z calculated through

Biot-Savart's law. This takes up approximately 4/5 of the time spent on each object function evaluation in the current discretization of the domain.

However, neglecting time consumption with the thought that high performance computers should be used to do this, we can take note of the positive results seen in the above experiments. We have seen that under the assumption of low contrast difference between individual sub-domains, the optimization routine finds a close-to-optimal solution and even when large contrast exists, finds a solution within 5% relative error on the individual parameters. We have seen that given good initial guesses the optimization routine can successfully estimate simple sub-domains with different anisotropic conductivity. We have also seen that the optimization routine can identify a lack of anisotropy when observing the object function for each set of electrodes. The most promising feature of the optimization method is that it is almost invariant under Gaussian additive noise of up to 10%. Lastly we see that the amount of data used to estimate the parameters has a high influence on the accuracy of the resulting estimates. This is highly logical, as more data is always better. The results coincides with literature where in the case of 3D anisotropic conductivity reconstruction, it is said that at least 7 linearly independent currents are needed[WS11]. This number is, however, based on having to use an iterative algorithm for attaining a global distribution of the anisotropic conductivity. We can, however, conclude that at least 3 sets of electrodes are needed to estimate 2D-anisotropic conductivity distributions with prior knowledge on interior boundaries.

Using an optimization algorithm instead of an iterative algorithm gives the unique opportunity to find the actual conductivity instead of a scaled conductivity which current leading MREIT software package CoReHA 2.0 is capable of giving[JL12]. Also, there are no practically applicable iterative algorithms for anisotropic conductivity estimation. Knowing the true anisotropic conductivity of the interior of for instance the human brain can greatly improve any medical electro-shock treatment strategies used because of the ability to predict the current density and thus, as much as possible, avoid areas which are not desirable to probe with electric currents. In diagnostics of cancerous tissue there is little to gain from finding anisotropic conductivity compared to a scaled isotropic conductivity distribution.

CHAPTER 5

Future Work and Conclusion

5.1 Future Work

There are several more aspects of anisotropic conductivity estimation through MREIT that need to be addressed in the future. These include

- Local object function information.

- Uniqueness of inverse problem in compressed sensing.

- More complex geometries.

- Statistical accuracy of estimated parameters.

The first item consists of whether using local objective functions in the respective sub-domains to infer local changes in conductivity distribution. Because the Biot-Savart law is based on infinitesimal contributions which decay with the distance to the probe point, a local "bad" objective function inside a sub-domain with regards to all data sets, should be able to guide better starting guesses for the optimization routine within that sub-domain.

Compressed sensing is about using data-sets with missing data to attain global solutions. This is a vital point of interest in MREIT because of the inherent bad MR signal in skeletal tissue, air bubbles, gas-filled organs etc. Specifically when interested in brain imaging, is it then possible to have uniqueness and estimate the conductivity distribution in the outer layers of skull and skin from B_z-data only available in the interior regions where the MR signal is fine. In the CoReHA 2.0 package a choice of σ is made in these outer layers which then results in the scaled values in the interior. But is it possible to do the opposite and estimate σ in the outer layers without any local data. The uniqueness of B_z shown in this thesis would suggest that the answer is yes, however, experiments are required and validation of these is a subject on its own.

This thesis has only operated with very simple domain structures. Namely a background isotropic conductivity and two sub-domains of varying anisotropic conductivity. This in total amounts to 9 variables, when not using prior knowledge of isotropic v. anisotropic tissue. If practical use of this approach is attempted, many more different tissue types are needed to be modelled, thus increasing the amount of parameters to be estimated. Furthermore, 3D conductivity tensor distributions are required which increases the amount of parameters per sub-domain from 3 to 6.

Lastly, the question of how accurate the estimated parameters are is vital. Is it possible to assign confidence intervals to the estimated parameters and if so, how does this scale with the amount of parameters.

5.2   Conclusion

The thesis has shown how the physics of attaching electrodes to a conducting media and measuring the resulting phase changes resulting from the internally induced magnetic field by the use of a MR-scanner can provide a unique forward model given known anisotropic conductivity distribution inside the media. The thesis has also shown that it is possible, in simple domains, to estimate an anisotropic conductivity distribution using MREIT when applying at least three sets of electrodes. It has been shown that the solution parameters attained using the method of solving the inverse problem of MREIT by optimization is largely invariant under different noise levels or signal to noise ratios. It is shown that the geometry of the interior sub-domains influence how well the estimated conductivity parameters fit true parameters in the case of two pairs of electrodes. It has also been shown that solving the inverse problem of MREIT with the aim of constructing isotropic conductivities is a bad idea when the media exhibits anisotropic conductivities. It has also been shown that high contrast between conductivities of sub-domains results in bias on the estimation. The most essential knowledge that has been gained is of the importance of initial

guesses on parameters which have to be good for the optimization to reach a convergence close to the global minimum.

Theorems and Definitions

This section will briefly go through the theorems and definitions needed in the following section.

A.1   Lax-Milgram lemma

Assume, H a Hilbert space.

$$a : H \times H \to \mathbb{C},$$

a complex valued functional satisfying

(a) sesquilinearity: for $\alpha_1, \alpha_2, \beta_1, \beta_2 \in \mathbb{C}$ and $u, v \in H$
$$a(\alpha_1 u_1 + \alpha_2 u_2, v) = \alpha_1 a(u_1, v) + \alpha_2 a(u_2, v),$$
$$a(u, \beta_1 v_1 + \beta_2 v_2) = \bar{\beta}_1 a(u, v_1) + \bar{\beta}_2 a(u, v_2).$$

(b) boundedness: for $\gamma > 0$ and $u, v \in H$
$$\exists \gamma > 0 \; s.t. \forall u, v, \; |a(u, v)| \leq \gamma \|u\| \|v\|. \tag{A.1}$$

(c) coercivity for $\delta > 0$ and $u \in H$

$$\exists \delta > 0 \ s.t. \forall u, v, \ |a(u,u)| \geq \delta \|u\|^2. \tag{A.2}$$

Then for any continuous linear functional $L : H \to \mathbb{C}$, there is a unique u in H
s.t. $a(u,v) = L(v), \quad \forall v \in H$.
These are the conditions for complex valued vector spaces, however, the lemma
applies equally for real valued vector spaces, however the sesquilinearity becomes
bilinearity.

A.2   Definition of Sobolev space

First of all, the main space of interest is the Sobolev space, $H^1(\Omega)$, which is
defined as the space for which functions have bounded weak first derivatives.

$$H^1(\Omega) = \{w \ : \ \int_\Omega w^2 + |\nabla w|^2 \ dx < \infty\}. \tag{A.3}$$

The space is equipped with the inner product

$$(w,v)_{H^1(\Omega)} = \int_\Omega \nabla v \nabla w + vw \ dx, \tag{A.4}$$

and the norm

$$\|w\|_{H^1(\Omega)} = \left(\int_\Omega |\nabla w|^2 + w^2 \ dx. \right)^{\frac{1}{2}} \tag{A.5}$$

A.2.1   Trace theorem

The Trace theorem is an important theorem regarding functions in Sobolev
spaces and their behaviour on the boundary. It goes as following.
  Assume Ω bounded with the boundary $\partial\Omega \in C^1$.

Then there exists a bounded linear operator, T,

$$T \ : \ H^1(\Omega) \to L^2(\partial\Omega), \tag{A.6}$$

such that

$$Tu = u|_{\partial\Omega} \ \texttt{if} \ \ u \in H^1(\Omega) \cap C(\bar{\Omega}), \tag{A.7}$$
$$\|Tu\|_{L^2(\partial\Omega)} \leq c\|u\|_{H^1(\Omega)}. \tag{A.8}$$

A.3 Hölder's inequality

For functions , w and v defined on a vector space associated with an inner product, the following inequality is fruitful. For, $1 \leq q, p < \infty$ where $\frac{1}{q} + \frac{1}{p} = 1$.

$$\int_\Omega |wv| \ dx \leq \left(\int_\Omega |w|^q \ dx \right)^{\frac{1}{q}} \left(\int_\Omega |v|^p \ dx \right)^{\frac{1}{p}}. \tag{A.9}$$

The special case of $q = p = 2$ is called Cauchy-Schwartz' inequality

$$\int_\Omega |wv| \ dx \leq \left(\int_\Omega |w|^2 \ dx \right)^{\frac{1}{2}} \left(\int_\Omega |v|^2 \ dx \right)^{\frac{1}{2}}. \tag{A.10}$$

Proof: Norm equivalence

Lemma:
The two norms

$$\|(u, U)\| = \inf_{c \in \mathbb{C}} (\|u - c\|^2_{H^1(\Omega)} + \|U - c\|^2_{\mathbb{C}^L})^{\frac{1}{2}}, \tag{B.1}$$

and

$$\|(u, U)\|_\star = \left(\|\nabla u\|^2_{L^2(\Omega)} + \sum_{l=1}^{L} \int_{e_l} |u(x) - U_l|^2 \, dS \right)^{\frac{1}{2}}, \tag{B.2}$$

are equivalent, i.e. for some constants $0 < \lambda < \Lambda < \infty$,

$$\lambda \|(u, U)\|_\star \leq \|(u, U)\| \leq \Lambda \|(u, U)\|_\star, \tag{B.3}$$

for all $(u, U) \in \dot{H}$.
Proof:

We start by showing the first inequality. For $(u, U) \in \dot{H}$, we choose a constant $c \in \mathbb{C}$, s.t.

$$\|u - c\|_{H^1(\Omega)}^2 + \|U - c\|_{\mathbb{C}^L}^2 < \|(u, U)\|^2 + \epsilon, \tag{B.4}$$

for arbitrary $\epsilon > 0$. We then modify the rhs. of (B.2) to

$$\|(u, U)\|_\star^2 = \|\nabla(u - c)\|_{L^2(\Omega)}^2 + \sum_{l=1}^{L} \int_{e_l} |u(x) - c - (U_l - c)|^2 \, dS \tag{B.5}$$

$$\leq \|\nabla(u - c)\|_{L^2(\Omega)}^2 + 2\sum_{l=1}^{L} \int_{e_l} |u(x) - c|^2 \, dS + 2\sum_{l=1}^{L} |e_l| |U_l - c|^2. \tag{B.6}$$

Here we have used the inequality $2ab \leq a^2 + b^2$. By the continuous embedding of $H^{1/2}(\partial\Omega) \subset L^2(\partial\Omega)$, the second term on the right can be bounded by

$$2\sum_{l=1}^{L} \int_{e_l} |u(x) - c|^2 \, dS \leq 2\|u - c\|_{L^2(\partial\Omega)}^2. \tag{B.7}$$

Then by the trace theorem, (A.8), (B.7) becomes

$$2\sum_{l=1}^{L} \int_{e_l} |u(x) - c|^2 \, dS \leq 2\|u - c\|_{L^2(\partial\Omega)}^2 \tag{B.8}$$

$$\leq C\|u - c\|_{H^1(\Omega)}^2. \tag{B.9}$$

Now, by inserting (B.9) in to (B.6) we obtain, when remembering from before that $C \geq 2$

$$\|(u, U)\|_\star^2 \leq \|\nabla(u - c)\|_{L^2(\Omega)}^2 + C\|u - c\|_{H^1(\Omega)}^2 + 2\sum_{l=1}^{L} |e_l||U_l - c|^2 \tag{B.10}$$

$$\leq \|\nabla(u - c)\|_{L^2(\Omega)}^2 + C\|\nabla(u - c)\|_{L^2(\Omega)}^2 + C\|u - c\|_{L^2(\Omega)}^2 + 2\|U - c\|_{\mathbb{C}^L}^2 \tag{B.11}$$

$$\leq (1 + C)\|\nabla(u - c)\|_{L^2(\Omega)}^2 + C\|\nabla(u - c)\|_{L^2(\Omega)}^2 + 2\|U - c\|_{\mathbb{C}^L}^2 \tag{B.12}$$

$$\leq (1 + C)\|\nabla(u - c)\|_{H^1(\Omega)}^2 + 2\|U - c\|_{\mathbb{C}^L}^2 \tag{B.13}$$

$$\leq C\left(\|\nabla(u - c)\|_{H^1(\Omega)}^2 + \|U - c\|_{\mathbb{C}^L}^2\right). \tag{B.14}$$

Then by (B.4) we see that

$$\|(u, U)\|_\star^2 \leq C(\|(u, U)\|^2 + \epsilon). \tag{B.15}$$

As this holds for arbitrary ϵ, the first part of inequality (B.3) shown. The Next part of the inequality is a little more tricky and requires a proof using contradiction. If

$$\|(u, U)\| \leq \Lambda\|(u, U)\|_\star, \tag{B.16}$$

is not true, then we can pick a sequence (u^n, U^n), $n = 1, 2..\infty$ of elements in $\dot{H}$ so

$$\|(u^n, U^n)\| = 1, \qquad \text{and} \qquad \|(u^n, U^n)\|_\star < \frac{1}{n}. \tag{B.17}$$

We then let $\{c^n\}_{n=1}^{\infty}$ be a sequence of constants chosen such that the sequence $(w^n, W^n) = (u^n - c^n, U^n - c^n)$ satisfies

$$1 \leq \|w^n\|_{H^1(\Omega)}^2 + \|W^n\|_{\mathbb{C}^L}^2 < 1 + \frac{1}{n}. \tag{B.18}$$

Then by the compact embedding theorem of Sobolev spaces over bounded domains, $\{w^n\}$ contains a weakly convergent subsequence, which for simplicity is

also denoted $\{w^n\}$, such that

$$w^n \rightarrow w \qquad \text{in } L^2(\Omega) \text{ for } n \rightarrow \infty, \tag{B.19}$$

for some $w \in L^2(\Omega)$. However, due to the definition of $\|(u^n, U^n)\|_\star$, since

$$\|\nabla w^n\|_{L^2(\Omega)} \leq \|(u^n, U^n)\|_\star < \frac{1}{n}, \tag{B.20}$$

then $\{w^n\}$ forms a Cauchy sequence in $H^1(\Omega)$ and converges with the limit $\nabla w = 0 \Rightarrow w = \text{const} = c_0$. From (B.20), noting that $\frac{1}{n} > \sqrt{k} \Rightarrow \frac{1}{n} > k$, we have that

$$\frac{1}{n} > \int_{e_l} |u^n(x) - U_l^n|^2 dS = \int_{e_l} |w^n(x) - c_0 + c_0 - W_l^n|^2 \, dS \tag{B.21}$$

$$= \int_{e_l} |w^n(x) - c_0|^2 dx - 2(\bar{W}_l^n - \bar{c}_0) \int_{e_l} (w^n(x) - c_0) \, dx + |W_l^n - c_0|^2 |e_l| \tag{B.22}$$

$$\geq -2|W_l^n - c_0| \int_{e_l} |w^n(x) - c_0| dS + |W_l^n - c_0|^2 |e_l| \Leftrightarrow \tag{B.23}$$

$$|e_l||W_l^n - c_0|^2 < \frac{1}{n} + 2|W_l^n - c_0| \int_{e_l} |w^n(x) - c_0| dS. \tag{B.24}$$

The factor $2|W_l^n - c_0|$ can be estimated by using (B.18) and applying the trace theorem (A.8) so that

$$|e_l||W_l^n - c_0|^2 \leq \frac{1}{n} + 2\left(1 + \frac{1}{n} + |c_0|\right) |e_l|^{\frac{1}{2}} \|w^n - c_0\|_{L^2(\partial\Omega} \tag{B.25}$$

$$\leq \frac{1}{n} + 2C\left(1 + \frac{1}{n} + |c_0|\right) |e_l|^{\frac{1}{2}} \|w^n - c_0\|_{H^1(\Omega)}. \tag{B.26}$$

Now, since $w^n \rightarrow c_0$ in $H^1(\Omega)$, (B.26) shows that $W_l^n \rightarrow c_0$ for $n \rightarrow \infty$. This poses a contradiction, because

$$1 = \|(u^n, U^n)\|^2 \leq \|w^n - c_0\|^2_{H^1(\Omega)} + \|W^n - c_0\|^2_{\mathbb{C}^L} \rightarrow 0. \tag{B.27}$$

Thus, the assumption that (B.16) was false, is wrong and the norms are equivalent.

Model testing

This appendix contains the set of plots created at the mesh sizes given by table 3.1. The plots contain individual potential- and current distributions together with the differences between the two solution methods for both the potential and the current solutions.

**(a)** Solution, $u(\mathbf{x})$, from CEM, mesh size of 19600 triangles

(b) Solution, $u(\mathbf{x})$, from Pure Robin Model, mesh size of 19600 triangles
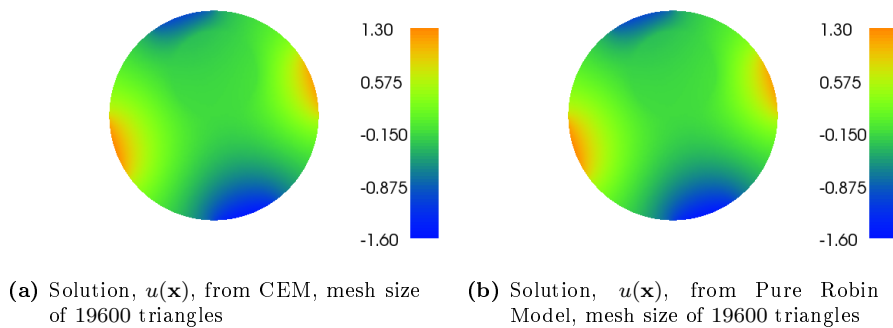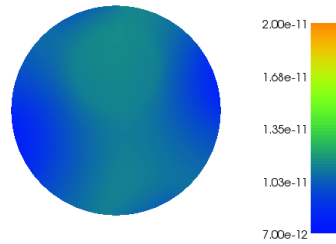
Figure C.1

Figure C.2: Difference between the solution for the potential from the two different models, i.e. $u_{CEM}(\mathbf{x}) - u_{Rob}(\mathbf{x})$, mesh size of 19600 triangles
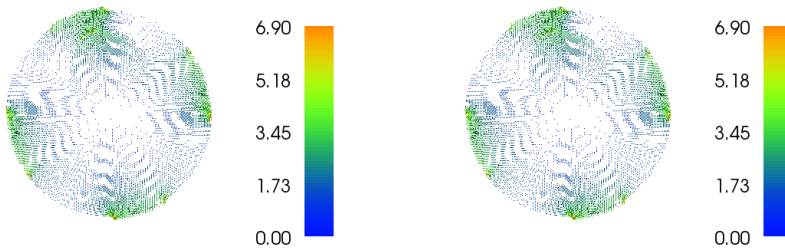
(a) Solution, $J(\mathbf{x})$, from CEM, mesh size of 19600 triangles

**(b)** Solution, $J(\mathbf{x})$, from Pure Robin Model, mesh size of 19600 triangles

Figure C.3
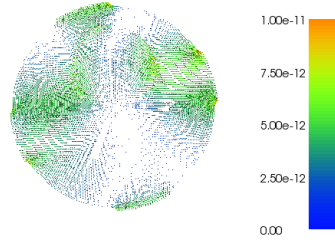
Figure C.4: Difference between the solution for the current, $-\sigma \nabla u$, from the two different models, i.e. $\mathbf{J}_{CEM}(\mathbf{x}) - \mathbf{J}_{Rob}(\mathbf{x})$, mesh size of 19600 triangles
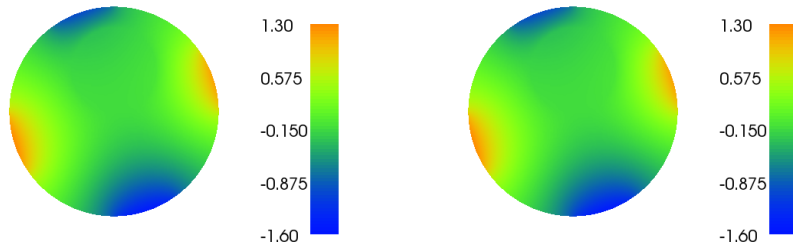
(a) Solution, $u(\mathbf{x})$, from CEM, mesh size of 40000 triangles

(b) Solution, $u(\mathbf{x})$, from Pure Robin Model, mesh size of 40000 triangles

Figure C.5
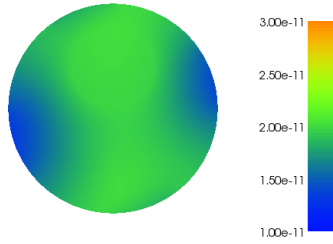
Figure C.6: Difference between the solution for the potential from the two different models, i.e. $u_{CEM}(\mathbf{x}) - u_{Rob}(\mathbf{x})$, mesh size of 40000 triangles
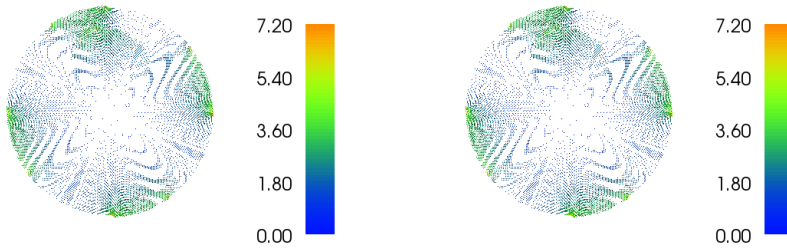
(a) Solution, $J(\mathbf{x})$, from CEM, mesh size of 40000 triangles

(b) Solution, $J(\mathbf{x})$, from Pure Robin Model, mesh size of 19600 triangles

Figure C.7
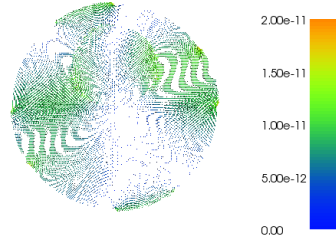
Figure C.8: Difference between the solution for the current, $-\sigma\nabla u$, from the two different models, i.e. $J_{CEM}(\mathbf{x}) - J_{Rob}(\mathbf{x})$, mesh size of 40000 triangles
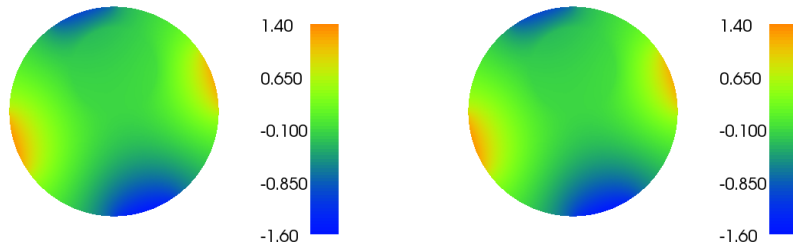
(a) Solution, $u(\mathbf{x})$, from CEM, mesh size of 67600 triangles

(b) Solution, $u(\mathbf{x})$, from Pure Robin Model, mesh size of 67600 triangles

Figure C.9
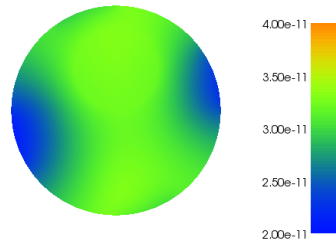
Figure C.10: Difference between the solution for the potential from the two different models, i.e. $u_{CEM}(\mathbf{x}) - u_{Rob}(\mathbf{x})$, mesh size of 67600 triangles
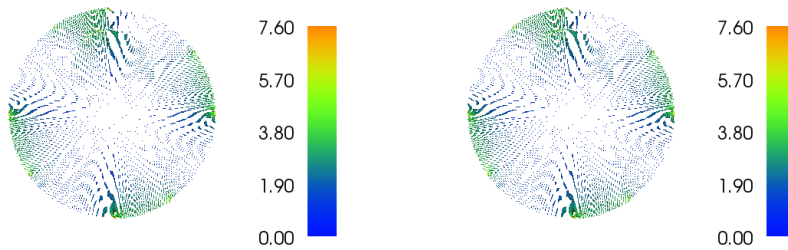
(a) Solution, $J(\mathbf{x})$, from CEM, mesh size of 67600 triangles

(b) Solution, $J(\mathbf{x})$, from Pure Robin Model, mesh size of 67600 triangles

Figure C.11
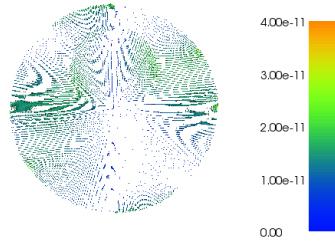
Figure C.12: Difference between the solution for the cur-
rent, $-\sigma\nabla u$, from the two different models, i.e.
$J_{CEM}(\mathbf{x}) - J_{Rob}(\mathbf{x})$, mesh size of 67600 triangles
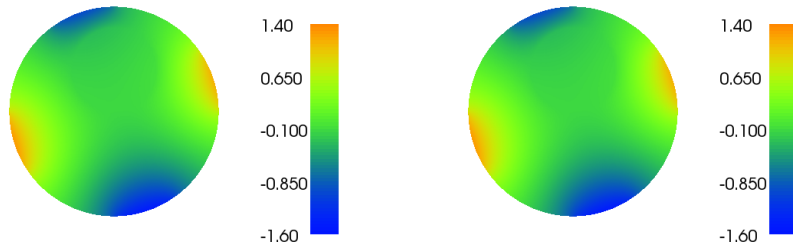
(a) Solution, $u(\mathbf{x})$, from CEM, mesh size
of 102400 triangles

(b) Solution, $u(\mathbf{x})$, from Pure Robin
Model, mesh size of 102400 triangles

Figure C.13
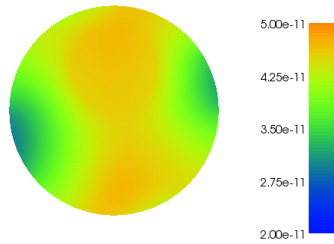
Figure C.14: Difference between the solution for the potential from the two different models, i.e. $u_{CEM}(\mathbf{x}) - u_{Rob}(\mathbf{x})$, mesh size of 102400 triangles
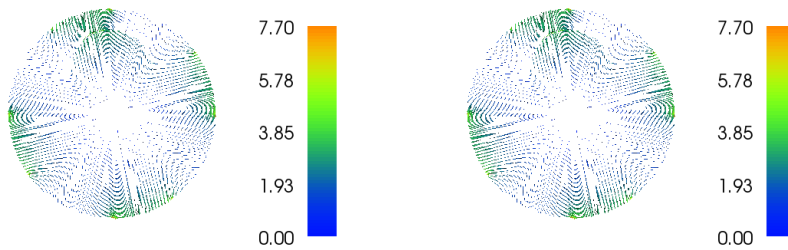
(a) Solution, $J(\mathbf{x})$, from CEM, mesh size of 102400 triangles

(b) Solution, $J(\mathbf{x})$, from Pure Robin Model, mesh size of 102400 triangles

Figure C.15
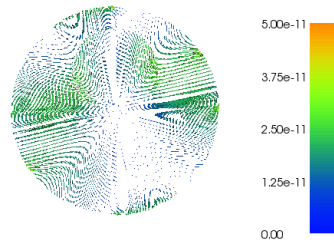
Figure C.16: Difference between the solution for the current, $-\sigma \nabla u$, from the two different models, i.e. $J_{CEM}(\mathbf{x}) - J_{Rob}(\mathbf{x})$, mesh size of 102400 triangles

Time Harmonic Derivation

Instead of looking for time independent solutions to Maxwell's equations, we can look for time harmonic solutions, i.e. we look for solutions where the vector fields are given by [SCI92]

$$\mathbf{E} = \tilde{\mathbf{E}}e^{i\omega t},$$
$$\mathbf{H} = \tilde{\mathbf{H}}e^{i\omega t},$$
$$\mathbf{B} = \tilde{\mathbf{B}}e^{i\omega t},$$
$$\mathbf{D} = \tilde{\mathbf{B}}e^{i\omega t},$$
$$\mathbf{J} = \tilde{\mathbf{J}}e^{i\omega t}.$$

where i, is the imaginary unit, ω is the frequency and t is the time parameter. (2.1) and (2.3) then become(excluding the tildes)

$$\nabla \times \mathbf{E} = -i\omega \mathbf{B}, \tag{D.1}$$
$$\nabla \times \mathbf{H} = \mathbf{J} + i\omega \mathbf{D}. \tag{D.2}$$

Next all the vector fields can be expanded in the magnetic permeability, assuming that $\mu << 1$ which is not a problem, since the magnetic permeability rarely changes much from the magnetic permeability in vacuum, $\mu_0 = 4\pi \cdot 10^{-7}$. Expansions of the fields goes as following.

$$\begin{aligned}
\mathbf{E} &= \mathbf{E}_0 + \mu\mathbf{E}_1 + ... \, , \\
\mathbf{H} &= \mathbf{H}_0 + \mu\mathbf{H}_1 + ... \, , \\
\mathbf{B} &= \mathbf{B}_0 + \mu\mathbf{B}_1 + ... \, , \\
\mathbf{D} &= \mathbf{D}_0 + \mu\mathbf{D}_1 + ... \, , \\
\mathbf{J} &= \mathbf{J}_0 + \mu\mathbf{J}_1 + ... \, .
\end{aligned}$$

Now, from (D.1) and (2.6), the zero-order equation becomes

$$\nabla \times \mathbf{E}_0 = 0,$$

which again implies the existence of a potential satisfying

$$\mathbf{E}_0 = -\nabla u.$$

Again, by taking the divergence of (D.2) and inserting (2.7) and (2.5) yields the zero order equation

$$\begin{aligned}
\nabla \cdot (\nabla \times \mathbf{H}) &= -\nabla \cdot (\sigma\nabla u + i\omega\epsilon\nabla u) \Leftrightarrow \\
0 &= -\nabla \cdot ((\sigma + i\omega\epsilon) \cdot \nabla u) = -\nabla \cdot (\kappa\nabla u).
\end{aligned}$$

Bibliography

[AF03]   Robert A. Adams and John J. F. Fournier. *Sobolev spaces*, volume 140 of *Pure and Applied Mathematics (Amsterdam)*. Elsevier/Academic Press, Amsterdam, second edition, 2003.

[ALM$^+$09] M.S. Alnaes, A. Logg, K.-A. Mardal, O. Skavhaug, and H.P. Langtangen. Unified framework for finite element assembly. *Internation Journal of Computational Science and Engineering*, 4, 2009.

[ALO$^+$13] Martin S. Alnaes, Anders Logg, Kristian B Oelgaard, Marie E. Rognes, and Garth N. Wells. Unified form language: A domain-specific language for weak formulations of partial differential equations. *ACM Transactions on Mathematical Software*, 2013.

[BLN95]   R. H. Byrd, P. Lu, and J. Nocedal. A limited memory algorithm for bound constrained optimization. *SIAM*, 16:1190–1208, 1995.

[DHK11]   Fabrice Delbary, Per Christian Hansen, and Kim Knudsen. Electrical impedance tomography: 3d reconstructions using scattering transforms. *Applicable Analysis: An International Journal*, 91:4:737–755, 2011.

[Eva10]   Lawrence C. Evans. *Partial Differential Equations*. American Mathematical Society, 2010.

[JL12]   Kiwan Jeon and Chang-Ock Lee. Cstudy 2.0: A software package for in vivo mreit experiments. *National Institute for Mathematical Sciences*, pages 305–811, 2012.

[JM10]   B. Jin and P. Maass. An analysis of electrical impedance tomography with applications to tikhonov regularization. *DFG*, 1324, 2010.

[KH98]   Per W. Karlsson and Vagn Lundsgaard Hansen. *Matematisk analyse 2*. Institute for Mathematics, Danish University of Technology, 1998.

[Kir04]   Robert C. Kirby. equations 839: Fiat, a new paradigm for computing finite element basis functions. *ACM Transactions on Mathematical Software*, 30:502–516, 2004.

[KL06]   Robert C. Kirby and Anders Logg. A compiler for variational forms. *ACM Transactions on Mathematical Software*, 32:417–444, 2006.

[LMea12]   A. Logg, K.-A. Mardal, and G. N. Wells et al. *Automated Solution of Differential Equations by the Finite Element Method*. Springer, 2012.

[LW10]   Anders Logg and Garth N. Wells. Dolfin: Automated finite element computing. *ACM Transactions on Mathematical Software*, 37, 2010.

[MWT11]   Alexander Opitz Mirko Windhoff and Axel Thielscher. Electric field calculations in brain stimulation based on finite elements: An optimized processing pipeline for the generation and usage of accurate individual head models. *Wiley Periodicals, Inc.*, 2011.

[PPKW04]   J. K. J. K. Seo. C. Pyo, C. Park, O. Kwon, and E.J. Woo. Image reconstruction of anisotropic conductivity tensor distribution in mreit: Computer simulation study. *Phys. Med. Biol.*, 49:4371–4382, 2004.

[SCI92]   Erkki Somersalo, Margaret Cheney, and David Isaacson. Existence and uniqueness for electrode models for electric current computed tomography. *SIAM*, 52:1023–1040, 1992.

[Uhl]   Gunther Uhlmann. The dirichlet to neumann map and inverse problems. *www.ipam.ucla.edu*.

[wea13]   Weak convergence (hilbert spaces), March 2013.

[WS08]   Eung Je Woo and Jin Keun Seo. Magnetic resonance elelectric impedance tomography (mreit) for high-resolution conductivity imaging. *Physiological Measurement*, 29:R1–R26, 2008.

[WS11]   Eung Je Woo and Jin Keun Seo. Magnetic resonance electrical impedance tomography (mreit). *SIAM*, 53(1):40–68, 2011.

[WS12]   Thomas Widlak and Otmar Scherzer. Hybrid tomography for conductivity imaging. *Inverse Problems*, 28(8):084008, 2012.

[YFF11]   Hugh D. Young, Roger A. Freedman, and A. Lewis Ford. *University Physics with Modern Physics*. Addison-Wesley, 2011.